### Title

Microtubules promote the non-cell autonomous action of microRNAs by inhibiting their cytoplasmic loading onto ARGONAUTE1 in Arabidopsis




### Journal

Developmental Cell, 57(8)

### ISSN

1534-5807



### Authors

Fan, Lusheng
Zhang, Cui
Gao, Bin
et al.



### Publication Date

2022-04-01

### DOI

10.1016/j.devcel.2022.03.015

Peer reviewed

HHS Public Access

Author manuscript

*Dev Cell*. Author manuscript; available in PMC 2023 April 25.

Published in final edited form as:

*Dev Cell*. 2022 April 25; 57(8): 995–1008.e5. doi:10.1016/j.devcel.2022.03.015.

# Microtubules promote the non-cell autonomous action of microRNAs by inhibiting their cytoplasmic loading onto ARGONAUTE1 in *Arabidopsis*

**Lusheng Fan**[1], **Cui Zhang**[2], **Bin Gao**[1], **Yong Zhang**[1], **Ethan Stewart**[3], **Jakub Jez**[3], **Keiji Nakajima**[4], **Xuemei Chen**[1,5,*]

[1]Department of Botany and Plant Sciences, Institute of Integrative Genome Biology, University of California, Riverside

[2]Key Laboratory of Plant Molecular Physiology, Institute of Botany, Chinese Academy of Sciences, Beijing 100093, China

[3]Vienna Biocenter Core Facilities (VBCF), Vienna, Austria

[4]Graduate School of Science and Technology, Nara Institute of Science and Technology, 8916-5 Takayama, Ikoma, Nara 630-0192, Japan

[5]Lead contact

## SUMMARY

Mobile microRNAs (miRNAs) serve as local and long-distance signals in developmental patterning and stress responses in plants. However, mechanisms governing the non-cell autonomous activities of miRNAs remain elusive. Here, we show that mutations that disrupt microtubule dynamics are specifically defective for the non-cell autonomous actions of mobile miRNAs, including miR165/6 that is produced in the endodermis and moves to the vasculature to pattern xylem cell fates in Arabidopsis roots. We show that KTN1, a subunit of a microtubulesevering enzyme, is required in source cells to inhibit the loading of miR165/6 into ARGONUATE1 (AGO1), which is cell-autonomous, to enable the miRNA to exit the cell. Microtubule disruption enhances the association of miR165/6 with AGO1 in the cytoplasm. These findings suggest that, while cell-autonomous miRNAs load onto AGO1 in the nucleus, cytoplasmic AGO1 loading of mobile miRNAs is a key step regulated by microtubules to promote the range of miRNA cell-tocell movement.

## Graphical Abstract

*Correspondence: xuemei.chen@ucr.edu.

AUTHOR CONTRIBUTIONS

X.C. and L.F. designed the experiments. X.C. supervised the project. L.F., C.Z., B.G. and Y.Z. performed the experiments. L.F., E.S. and J.J. analyzed the data. X.C., L.F. and K.N. wrote the manuscript.



DECLARATION OF INTERESTS

The authors declare no competing interests.

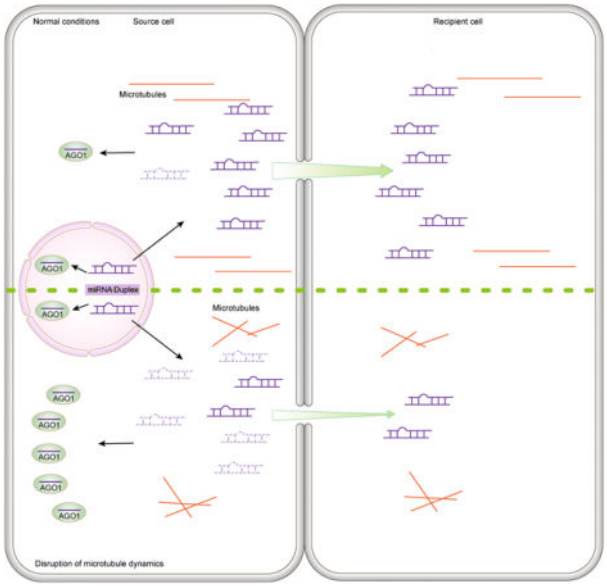


## Abstract

MicroRNAs act non-cell autonomously as mobile signals in various plant developmental processes. Fan et al. showed that KTN1, a microtubule severing enzyme, promotes the non-cell autonomous activities of microRNAs through inhibiting their loading onto AGO1 in the cytoplasm.

## INTRODUCTION

MicroRNAs (miRNAs) are 20–24-nucleotide (nt) long, non-coding RNAs that regulate nearly all aspects of plant life via posttranscriptional gene silencing (Bologna and Voinnet, 2014; Yu et al., 2019). In plants, the entire miRNA biogenesis process including *MIR* gene transcription, primary miRNA (pri-miRNA) processing, methylation of miRNA/miRNA* duplexes and their loading onto ARGONUATE1 (AGO1), and the formation of RNA-induced silencing complexes (RISCs) is thought to occur in the nucleus. miRISCs are then exported to the cytoplasm (Bologna et al., 2018), where they recognize target mRNAs via a high degree of sequence complementarity, leading to (1) transcript cleavage through the endonuclease activity of AGO1, or (2) translational inhibition (Baumberger and Baulcombe, 2005; Brodersen et al., 2008; Li et al., 2013).

A key feature of RNA silencing mediated by small RNAs is non-cell autonomous action, in which a silencing signal moves locally (cell to cell) and systemically (over a long distance) (Chen and Rechavi, 2021; Chitwood et al., 2009; Klesen et al., 2020; Melnyk et al., 2011). Small RNAs, including transgene and endogenous small interfering RNAs (siRNAs) and miRNAs, have been recognized as the mobile signals (Buhtz et al., 2010; Lewsey et al., 2016; Li et al., 2021; Lin et al., 2008; Molnar et al., 2010; Zhang et al., 2014). Mobile small RNAs may coordinate events in distant plant parts. For example, several miRNAs are induced in shoots and transported to roots to regulate responses to nutrient starvation and nodulation (Buhtz et al., 2010; Lin et al., 2008; Okuma et al., 2020; Pant et al., 2008).

Mobile small RNAs, such as miR165/6, miR394, and the trans-acting siRNA tasiR-ARF, serve as morphogenic signals that pattern cell fates in development (Carlsbecker et al., 2010; Chitwood et al., 2009; Knauer et al., 2013; Miyashima et al., 2011). In roots, *MIR165/6* genes are specifically expressed in the endodermis, but miR165/6 forms an activity gradient towards the center of the vasculature, which leads to an opposing gradient in the expression of its target gene *PHABULOSA* (*PHB*) (Carlsbecker et al., 2010; Miyashima et al., 2011). Cells in the vasculature with the highest level of *PHB* expression become metaxylem while neighboring cells with lower levels of *PHB* expression adopt the protoxylem fate. The mobile agents in non-cell autonomous RNA silencing by transgenes are likely siRNA duplexes (Devers et al., 2020). As AGO1 is cell-autonomous, the movement of siRNA duplexes from cell to cell is negated by their loading onto AGO1 during transit (Devers et al., 2020). Previous studies show that miRNAs spread through the plasmodesmata in *Arabidopsis* and generate a gradient distribution pattern consistent with passive diffusion between cells (Chitwood et al., 2009; Skopelitis et al., 2017; Vaten et al., 2011). However, it was also observed that the cell-to-cell movement of miRNAs is directional at some cell-cell interfaces, implicating regulated mobility (Skopelitis et al., 2018). A modeling approach showed that diffusion alone cannot account for the miR165/6 activity gradient (Muraro et al., 2014). Mechanisms that regulate the cell-to-cell movement of small RNAs are largely unknown.

Microtubules (MTs) are dynamic structures. They constantly grow and shrink at their two ends through polymerization and depolymerization. They may undergo treadmilling under conditions that favor net growth at the plus end and net loss at the minus end. MT dynamics is tightly regulated by MT-associated proteins (MAP), such as MICROTUBULE ORGANIZATION 1 (MOR1), a homolog of the conserved MAP215 family, which is required for the rapid shrinkage and growth of MTs (Kawamura and Wasteneys, 2008). The Arabidopsis KATANIN1 (KTN1) gene encodes the p60 subunit of Katanin, which severs MTs at crossover sites to maintain organized MT arrays and to ensure dynamic MT re-organization in the cytosol (Lin et al., 2013). The dynamic MT cytoskeleton plays pivotal roles in multiple fundamental cellular processes (Ehrhardt and Shaw, 2006), including the cell-to-cell movement of Tobacco Mosaic Virus (Boyko et al., 2007). Interestingly, KTN1 was also found to be required for the translation repression, but not the RNA cleavage, activity of plant miRNAs, suggesting that MT dynamics regulates miRNA activities (Brodersen et al., 2008). It is unknown whether MTs are required for the cell-to-cell movement of miRNAs.

Here, we show that mutations in *KTN1* and *MOR1* compromise the cell-to-cell movement of miRNAs in leaves and roots. In roots, the mutants exhibit xylem patterning defects reminiscent of reduced mobility of miR165/6, which is also reflected by a shallower *PHB* gradient. More importantly, we show that, while critical for the non-cell autonomous action of miR165/6, *KTN1* is dispensable for the cell-autonomous activity of the miRNA. Furthermore, *KTN1* is required in cells in which miR165/6 is made (endodermis) but dispensable in destination cells (metaxylem). Through tissue-specific analysis of AGO1 loading, we found that *KTN1* inhibits the loading of miR165/6 onto AGO1 in the source tissue, thus promoting its exit. Disruption of MTs enhances the loading of miR165/6 onto AGO1 in the cytoplasm. These findings reveal that, while cellautonomous miRNAs undergo

AGO1 loading in the nucleus, cytoplasmic AGO1 loading is a key point of regulation for mobile miRNAs and that MTs inhibit cytoplasmic RISC formation to promote the non-cell autonomous action of miRNAs.

## RESULTS

### Identification of KTN1 as a potential regulator of the non-cell autonomous activities of miRNAs

We performed an ethyl methanesulfonate mutagenesis screen using the *SUC2::amiR-SUL* (*amiR*) transgenic line, in which the amiR-SUL artificial miRNA is specifically produced in companion cells in the phloem and non-cell autonomously silences the *SULFUR* (*SUL*) gene in leaf mesophyll cells, leading to vein-centered leaf chlorosis (de Felippes et al., 2011). We isolated a mutant with reduced leaf bleaching, which implies compromised amiR-SUL activity (Figure 1A). The mutant exhibited morphological phenotypes reminiscent of mutants in *KATANIN1* (*KTN1*), such as smaller and rounder leaves (Figure 1A). Indeed, a point mutation at the splice site of the first intron of *KTN1* was identified in this mutant and termed *ktn1-20* (Figure S1A). Another *ktn1* mutant with a T-DNA insertion, *ktn1-2* (Figure S1A), also led to weaker chlorosis when introduced into *amiR* (Figure 1A). A genomic fragment containing the promoter and coding region of *KTN1* fully rescued the developmental and leaf chlorosis phenotypes of *amiR ktn1-20*, confirming that loss of function in *KTN1* was responsible for these phenotypes (Figure 1B).

The weaker leaf chlorosis of *amiR ktn1-20* could be due to compromised miRNA biogenesis. RNA gel blot assays showed that the levels of amiR-SUL and miR168 were similar between *amiR ktn1-20* and *amiR* (Figure S1B). Small RNA-seq with *ktn1-20* and wild type did not find global changes in miRNA abundance in the mutant (Figure S1 C–E, Table S2), which ruled out a general role of *KTN1* in miRNA biogenesis. Real-time RT-PCR analysis showed that *SUL* transcript levels were similar in *amiR ktn1-20* and *amiR* (Figure 1C). The levels of the SUL protein were lower in *amiR* than in wild type (Col-0), as expected, and higher in *amiR ktn1-20* than in *amiR* (Figures 1D and S1G). Thus, these data are consistent with previous findings that *KTN1* mediates the translation repression activity of plant miRNAs (Brodersen et al., 2008).

We next asked whether the *ktn1-20* mutation resulted in a reduced range of movement of amiR-SUL, which would be reflected by a narrow span of bleaching around the veins. We used Open CV (Bradski and Kaehler, 2000) to quantify the spatial patterns of leaf bleaching (Figure 1E; see Methods). At the level of whole leaves, the severity of bleaching was significantly alleviated in *amiR ktn1-20* relative to *amiR*, consistent with visual inspection (Figure 1F). The area of bleaching along the vasculature, representing the range of non-cell autonomous action of amiRSUL, was significantly reduced in the *amiR ktn1-20* mutant, even after normalization to total leaf area (Figure 1G). Interestingly, in addition to the increased hue value near the veins, the hue value in inter-vein areas was also remarkably increased in *amiR ktn1-20* (Figures 1H and 1I), which indicates reduced bleaching in both vein and inter-vein areas. This suggests that amiRSUL's range of movement in *amiR* was likely broader than the distance of 15 cells from the veins as previously reported (de Felippes et al., 2011). The strong silencing near veins and weaker silencing in inter-vein

regions in *amiR* are reminiscent of the threshold effects observed for the activities of mobile miR165/6 and tasiR-ARF in leaves (Chitwood et al., 2009; Merelo et al., 2016; Skopelitis et al., 2017).

To definitively show that *KTN1* is required for the cell-to-cell movement of amiR-SUL, we mechanically separated leaf vascular, mesophyll and epidermal tissues by Meselect (Svozil et al., 2016) and examined amiR-SUL levels in source (vascular) and recipient (mesophyll and epidermal cells) tissues. Tissue enrichment was successful, as shown by the expression of *SUC2*, *CAB3*, and *ATML1*, which mark vascular, mesophyll, and epidermal tissues, respectively (Figures S2A, S2B and S2D). As expected, amiR-SUL was enriched in the vascular tissue in both *amiR* and *amiR ktn1-20* as compared to mesophyll and epidermal tissues. More importantly, the abundance of amiR-SUL was increased in the vascular tissue but decreased in mesophyll and epidermal tissues in *amiR ktn1-20* relative to *amiR* (Figures 1J, S2C and S2E), indicating reduced cell-to-cell movement of amiR-SUL in the *ktn1-20* background.

We employed *Arabidopsis* micrografting to examine whether *KTN1* impacts the long-distance movement of amiR-SUL. In wild type rootstocks micrografted onto *amiR* scions (*amiR*/WT), a substantial amount of amiR-SUL was detected, suggesting that amiR-SUL was able to move from shoot to root. The levels of amiR-SUL were similar in *amiR*/WT vs. *amiR*/*ktn1-20* rootstocks, suggesting that the long-distance trafficking of amiR-SUL was not impacted when the *ktn1-20* mutation was in the recipient tissue. Interestingly, the level of amiR-SUL in *amiR ktn1-20*/WT rootstocks was substantially lower than those in *amiR*/WT rootstocks (Figures 1K and S1H). These results demonstrated that *KTN1* is required in source tissues for the long-distance movement of amiR-SUL.

## KTN1 patterns xylem cell fates by enabling the non-cell autonomous function of miR165/6

We next evaluated whether *KTN1* promotes the non-cell autonomous activities of endogenous miRNAs. The well-characterized non-cell autonomous action of miR165/6 and the dosagedependent activity of the miRNA in the regulation of its target gene *PHB* leading to xylem patterning (Carlsbecker et al., 2010; Miyashima et al., 2011) provided a superb model for our purposes. First, we examined the xylem patterns in *ktn1-20*. There are two metaxylem files flanked by two protoxylem files in a wild-type root (Figure 2A). However, in *ktn1-20* roots, metaxylem was present, but protoxylem differentiation was severely impaired such that protoxylem was replaced by metaxylem or ectopic files of metaxylem were found (Figures 2B and 2F). Expression of *KTN1* under its native promoter fully rescued the xylem patterning defects, indicating that the impaired xylem development was due to the *ktn1-20* mutation (Figures 2C 2F). As xylem differentiation is controlled by *PHB* in a dosage-dependent manner: high and low levels of *PHB* specify metaxylem and protoxylem, respectively (Carlsbecker et al., 2010; Miyashima et al., 2011), we compared the *PHB* expression patterns between WT and *ktn1-20* (Figures S3A–S3L). In WT, PHB-GFP distribution formed a gradient across the stele, with the highest level in the center and a drastic decline towards the periphery (Figures 2G, 2I and S3JL). In contrast, the sharp gradient distribution was disrupted in *ktn1-20*, with more cell files showing high levels of PHB-GFP (Figures 2H, 2I and S3J–S3L), which was consistent with the higher numbers

of metaxylem. To rule out that miR165/6 biogenesis was affected in *ktn1-20*, we first examined the spatial expression patterns of *MIR165A*, *MIR165B*, *MIR166A* and *MIR166B*, the four out of nine *MIR165/6* genes with detectable expression in the root (Miyashima et al., 2011). The promoters of these genes drove the expression of GFP specifically in the endodermis in the root (Figure S4A). The *ktn1-20* mutation did not affect the tissue-specific promoter activities of the four genes (Figures S4A and S4B). The levels of all nine pri-miR165/6s were determined by qRT-PCR, and no significant changes were found for any transcript between WT and *ktn1-20* (Figure. S4C). RNA gel blot assays showed that miR165/6 accumulation was similar between WT and *ktn1-20* (Figure S4D), which was consistent with results from small RNA sequencing (Figure S1F). Previous studies showed that AGO10 specifically sequesters miR165/6 and promotes its degradation (Yu et al., 2017; Zhu et al., 2011). The xylem patterning defects in *ktn1-20* could be due to altered *AGO10* expression. Western blotting showed that the AGO10 protein level was not affected in *ktn1-20* (Figure S4E). We further examined the 3' truncation and 3' tailing of miR165/6, which are associated with miRNA degradation. Patterns of miR165a-b and miR166a-g in *ktn1-20* were identical to those in WT (Figure S4F). Taken together, these results indicate that *KTN1* is required for the non-cell autonomous function of miR165/6, but dispensable for its biogenesis or degradation.

## MOR1 is required for the non-cell autonomous actions of miRNAs

As *KTN1* is required for the formation of highly ordered microtubule arrays, we further examined the effects of another MT mutant, *mor1-1*, on the non-cell autonomous activities of miRNAs. The *mor1-1* allele is temperature sensitive: microtubules are shorter and less dynamic in *mor1-1* plants grown at the restrictive temperature (30°C) (Kawamura and Wasteneys, 2008; Whittington et al., 2001). *amiR mor1-1* showed no obvious leaf bleaching defects when grown under normal temperature (Figures 3A and 3C). However, when the plants were transferred to the restrictive temperature, newly emerged leaves showed reduced leaf bleaching in comparison to *amiR* (Figures 3B and 3C), while amiR-SUL levels in *amiR mor1-1* showed no significant changes relative to *amiR* under either normal or restrictive temperature (Figure 3D).

We further examined the xylem patterns of *mor1-1* grown under the restrictive temperature. Xylem differentiation into metaxylem and protoxylem was not affected in WT at 30 °C (Figures S3M and S3N). In contrast, metaxylem formed in the position of protoxylem or was increased in number in *mor1-1* plants grown under the restrictive temperature for 4 days (Figures S3M and S3N). The PHB-GFP gradient in the stele was unaffected in WT but was abolished in *mor1-1* at 16 hours after plants were transferred to 30°C (Figures S3L, S3O and S3P). More cell files expressed high levels of PHB-GFP in *mor1-1* at the restrictive temperature, consistent with the increased number of metaxylem cell files. The levels of miR165/6 were similar between WT and *mor1-1* under both normal and restrictive conditions (Figure S3Q).

It has been shown that *ktn1* mutant roots are wider than wild type roots (Webb et al., 2002), which was also observed for *ktn1-20* roots (Figures S3R and S3S). We considered the possibility that the enlarged root diameter rather than the disruption of MTs *per se* prevented

miR165/6 movement into the center of the stele. The temperature-sensitive nature of *mor1-1* provided an opportunity to examine the PHB-GFP gradient without the complication of enlarged root diameter. The graded PHB-GFP distribution was already disrupted in *mor1-1* (Figures S3O and S3P) at 16 hours after plants were transferred to the restrictive temperature when no change in root diameter was observed (Figures S3T and S3U). Note that the MT defects of *ktn1* and *mor1* mutants are not identical. In *ktn1* mutants, MTs show a network-like distribution (Lin et al., 2013), while in *mor1* mutants, MTs become short and less dynamic (Kawamura and Wasteneys, 2008; Whittington et al., 2001). Taken together, the effects of *ktn1* and *mor1* mutations on amiR-SUL and miR165/6 suggest that well-organized MTs or dynamic MTs play a vital role in the non-cell autonomous actions of miRNAs.

## KTN1 is dispensable for the cell autonomous activity of miR165/6

Although *KTN1* was shown to enable the non-cell autonomous activity of miR165/6 in repressing its target *PHB* in the stele, *KTN1* does not necessarily promote the cell-to-cell movement of miR165/6. An alternative possibility is that *KTN1* is required for the repression of miR165/6 target genes in stele cells that receive this mobile miRNA. To test this possibility, we expressed *MIR165A* under the *CRE1* promoter, which is active specifically in the stele (Carlsbecker et al., 2010) where the miR165/6 target *PHB* is expressed. In the WT root, expression of *MIR165A* in the stele led to the conversion of metaxylem to protoxylem (Figures 4A and 4B), consistent with the notion that low *PHB* expression specifies protoxylem (Carlsbecker et al., 2010; Miyashima et al., 2011). As in WT, expression of *MIR165A* in the stele resulted in ectopic protoxylem formation in *ktn1-20* (Figures 4A and 4C). We further introduced *PHB::PHB-GFP* into both *CRE1::MIR165A* and *CRE1::MIR165A ktn1-20* and found that the graded distribution of PHB-GFP was disrupted in both wild type and *ktn1-20* backgrounds, with very weak PHB-GFP signals evenly distributed in the stele (Figures 4D–4G). These results demonstrated that miR165 was functional in *ktn1-20* when expressed in the same tissues as its target *PHB*. Therefore, *KTN1* is not required for the cell-autonomous activity of miR165/6. *KTN1*-regulated microtubule organization was reported to be required for the spiral cell wall thickening in the protoxylem (Schneider et al., 2021). Our results here showed that expression of *MIR165A* in the stele results in ectopic formation of protoxylem cell wall patterns in the *ktn1-20* background, which suggests that KTN1's role in protoxylem cell wall patterning is likely indirect, properly through its regulation of xylem cell fates via miR165/6.

## KTN1 is required in the endodermis for the non-cell autonomous action of miR165/6

To explore how *KTN1* promotes the non-cell autonomous action of miR165/6, we expressed *KTN1* in various root cell layers using layer-specific promoters, including *EN7* (endodermis and weakly in the cortex), *AHP6* (protoxylem and adjacent pericycle), *ACL5* (metaxylem and procambia) and *SHR* (stele) (Figure 5A). Three independent T3 lines were analyzed for each construct. The xylem phenotypes varied among independent transformants of the same transgene, which may be due to the variability in expression levels of the transgenes and similar phenomena were also observed in other studies (Fan et al., 2021; Ursache et al., 2014). However, despite the variability, only *EN7::KTN1* fully rescued the xylem defects in *ktn1-20* as did *KTN1::KTN1* among these transgenes (Figures 5B and 5C). *AHP6::KTN1*

only partially rescued the xylem patterning defects (Figures 5B and 5C). In addition, neither *ACL5::KTN1* nor *SHR::KTN1* was able to rescue the xylem defects in *ktn1-20* (Figures 5B and 5C). These results support the conclusion that *KTN1* is specifically required for the non-cell autonomous action of miR165/6 in the source tissue.

## KTN1 inhibits the loading of miR165/6 onto AGO1 in source cells to promote its cell-to-cell movement

Previous studies show or implicate siRNA duplexes as the mobile agents in cell-to-cell movement (Devers et al., 2020). Furthermore, AGO1 expressed under various root layer-specific promoters are cell-autonomous (Brosnan et al., 2019); this study - see below), indicating that siRISCs or miRISCs are not cell-to-cell mobile. Thus, RISC formation is likely to inhibit the trafficking of small RNAs into neighboring cells. In fact, mobile siRNAs are increasingly depleted as they load onto AGO1 during their cell-to-cell transit (Devers et al., 2020). Given this knowledge, we sought to determine whether KTN1 affects the loading of miR165/6 onto AGO1 in source and recipient cells. We first generated transgenic lines expressing GFP-AGO1 under either *EN7* or *ACL5* promoters that are active in endodermis (and weakly in the cortex) (Heidstra et al., 2004) and metaxylem/procambium (Muniz et al., 2008), respectively (Figure 6A). *EN7::GFP-AGO1* signals were indeed strongest in the endodermis (with weak signals in the cortex) and *ACL5::GFP-AGO1* signals were only in the metaxylem (Figure 6B), consistent with AGO1 being cell-autonomous. Immunoprecipitation (IP) was performed using an anti-GFP antibody followed by protein gel blots to confirm the successful IP of GFP-AGO1 (Figure S5A). RNAs were isolated from the immunoprecipitates and subjected to small RNA-seq. As compared to Arabidopsis total small RNA profiles showing a prominent 24-nt peak and a smaller 21-nt peak (Li et al., 2016), in GFPAGO1 IP small RNA-seq, 21-nt small RNAs were enriched while 24-nt small RNAs were diminished (Figure S5B), indicating successful IP. The two biological replicates were highly correlated with each other for all the genotypes analyzed (Figures S5C–S5F). 10 differentially AGO1-associated miRNA species between *EN7::GFP-AGO1 ktn1-20* and *EN7::GFP-AGO1* (Figure S5G, Table S3) and 19 differentially AGO1-associated miRNA species between *ACL5::GFP-AGO1 ktn1-20* and *ACL5::GFP-AGO1* (Figure S5H, Table S4) were found. Among these miRNA species, AGO1-associated miR165/6 was at a higher level in the endodermis as compared to the metaxylem while AGO1-associated miR156 was at a lower level in the endodermis as compared to the metaxylem in both *ktn1-20* and wild type (Figure 6C), which is consistent with findings from a previous study (Brosnan et al., 2019). Strikingly, the abundance of AGO1-bound miR165/6 was higher in the endodermis but lower in the metaxylem in *ktn1-20* as compared to wild type (Figure 6C). The spatial distribution of miR166 was further examined by in situ hybridization. In wild type, miR166 signals were similar in the endodermis and the stele. But in *ktn1-20*, the signals in the stele were much lower as compared to those in the endodermis; the signals were also much lower than those in the stele in WT (Figure 6D). It is worth noting that only some of the *ktn1* individuals showed reduced miR166 signals in the stele, which is correlated with the incomplete penetrance of the xylem patterning defects of the mutant (Figure 2F). These results are consistent with the reduced trafficking of miR165/6 from the endodermis in the *ktn120* mutant, as well as with the observation that the association of miR165/6 with AGO1 in *ktn1-20* is lower in the metaxylem. These results suggest that

*KTN1* suppresses the loading of miRNA165/6 onto AGO1 in the endodermis. Given that AGO1 is cell-autonomous, we speculate that intact, dynamic microtubules suppress the association of miR165/6 with AGO1 in the endodermis to allow AGO1-unbound miR165/6 to exit the endodermis.

## MTs suppress the association of miR165/6 with cytoplasmic AGO1

In the process of miRNA biogenesis, miRNAs are loaded onto AGO1 in the nucleus and miRISCs are exported to the cytoplasm (Bologna et al., 2018). We sought to understand how *KTN1* suppresses the loading of miR165/6 onto AGO1. We first examined whether *KTN1* affects the nucleo-cytoplasmic partitioning of AGO1, as suppression of AGO1's nuclear import could perceivably inhibit miRISC formation during miRNA biogenesis in the nucleus. In *ktn1-20*, the steady-state GFP-AGO1 signals exhibited a diffuse pattern in the cytoplasm similar to those in wild type (Figure S6A). As the steady-state GFP-AGO1 localization did not reveal the nuclear pool of AGO1, we performed nuclear-cytoplasmic fractionation to examine the distribution of AGO1. Results showed that AGO1 protein levels were approximately the same between *ktn1-20* and wild type in either fraction (Figure S6B), indicating that *ktn1-20* did not affect the nuclear-cytoplasmic partitioning of AGO1. Similarly, RNA gel blot assays showed that *ktn1-20* did not alter the levels of eight examined miRNAs or their nucleo-cytoplasmic partitioning (Figure S6C). Thus, *KTN1* does not affect the nuclear import/export of AGO1 or miRISCs.

Given the formation of miRISCs in the nucleus during miRNA biogenesis, for mobile miRNAs, there must be an unloaded fraction that exits the nucleus and then the cell. It is unknown how mobile miRNAs avoid AGO1 loading in the cytoplasm in source cells. It is also unknown whether AGO1 loading occurs in the cytoplasm or the nucleus for mobile miRNAs that arrive in the cytoplasm of a recipient cell. Given that *KTN1* suppresses the loading of miR165/6 onto AGO1 without affecting the nucleo-cytoplasmic distribution of AGO1, we entertained the hypothesis that miR165/6 can be loaded onto AGO1 in the cytoplasm and *KTN1* suppresses this process. To test this, we fused the ligand-binding domain of mammalian glucocorticoid receptor (GR) to GFP-AGO1 to prevent its nuclear localization (Dittmar et al., 1997; Horstman et al., 2017). *35S::GRGFP-AGO1* was transiently co-expressed with *35S::MIR165A* and *35S::mScarlet-MAP4* (a marker for MTs) (Pan et al., 2020) in *N. benthamiana* leaves. GR-GFP-AGO1 and mScarlet-MAP4 signals were detected at 36 hours post infiltration. As expected, GR-GFP-AGO1 was exclusively localized in the cytoplasm and mScarlet-MAP4 signals reflected well organized cortical MT arrays (Figure 7A). We next tested whether miR165 could be loaded onto cytoplasmic AGO1 and whether MT organization affected cytoplasmic miRISC formation. MTs were disrupted by infiltrating the leaves with the MT depolymerization drug oryzalin at 36 hours after infiltration of the above constructs. After another 24 hours, MTs were fragmented and depolymerized, as indicated by mScarlet-MAP4 signals, while MTs were intact in mock-treated leaves (Figure 7A). The speed of cytoplasmic streaming was not affected 24 hours after oryzalin treatment (Figure S6D), confirming the viability of cells. We immunoprecipitated GR-GFP-AGO1 and analyzed the levels of miR165 associated with GR-GFP-AGO1 by RNA gel blot analysis. Indeed, miR165 was associated with cytoplasmic GR-GFP-AGO1, indicating that miRISC can form in the cytoplasm. Strikingly,

the association of miR165 with GR-GFP-AGO1 was enhanced in a time course after oryzalin application (Figures 7B and S6E). These results indicate that intact and/or dynamic MTs suppress the loading of miR165 onto AGO1 in the cytoplasm.

## DISCUSSION

In this study, we showed that MTs are required for the non-cell autonomous activities of miRNAs with the following lines of evidence: (1) In the *amiR* system, *ktn1* mutations reduce the area of leaf bleaching caused by the mobile amiR-SUL without affecting its accumulation; (2) A *ktn1* mutation abolishes the gradient distribution of PHB controlled by the miR165/6 gradient in the root (Carlsbecker et al., 2010; Miyashima et al., 2011), consequently compromising xylem patterning; (3) A mutation in the MT-associated protein MOR1 similarly affects the non-cell autonomous activities of amiR-SUL and miR165/6 as do *ktn1* mutations. Based on these results, we tentatively conclude that KTN1- and MOR1-regulated microtubule organization is critical to the non-cell autonomous actions of miRNAs.

*KTN1* was previously found to be required for the translation repression activities of miRNAs (Brodersen et al., 2008). Thus, the observed effects of *ktn1* mutations on amiR-SUL or miR165/6 could be explained by *KTN1* aiding their target repression activities rather than their cell-to-cell movement *per se*. However, we were able to show that *KTN1* promotes the cell-to-cell movement of amiR-SUL by measuring its levels in source and recipient tissues (Figures 1J and S2). We also showed that *KTN1* is required in shoots for the shoot-to-root trafficking of amiR-SUL (Figures 1K and S1H). Expression of *KTN1* in the endodermis (source of miR165/6) but not the metaxylem (destination of miR165/6) rescued the xylem defects in *ktn1*. These results collectively suggest that *KTN1* acts in source cells to enable the transport of miRNAs. Expression of *KTN1* in the protoxylem (tissue miR165/6 transits through) partially rescued the xylem defects, which suggests that *KTN1* may also play a role in intermediary tissue during the transport of miRNAs.

In plants, most miRNAs are associated with their effector protein AGO1. By gel filtration, a cytoplasmic pool of AGO1-unbound miRNAs was found (Dalmadi et al., 2019), suggesting that AGO1 loading is not 100% for certain miRNAs. AGO1 is cell-autonomous, as expression of fluorescent protein-tagged AGO1 with layer-specific promoters in the root resulted in corresponding layer-specific signals (Brosnan et al., 2019), which was also found in this study with *EN7::GFP-AGO1* and *ACL5::GFP-AGO1* lines. This indicates that AGO1-unbound miRNAs undergo cell-to-cell movement. In fact, AGO1 was found to “consume” mobile siRNAs as they traverse root cell layers by forming siRISCs to prevent their further movement (Devers et al., 2020). We found that the association of miR165/6 with AGO1 in the endodermis is higher in *ktn1* as compared to wild type, suggesting that *KTN1* suppresses miR165/6-AGO1 RISC formation in the endodermis to enable the exit of AGO1-unbound miR165/6.

In *Arabidopsis*, AGO1 contains a nuclear localization signal and a nuclear export signal that enable its nucleo-cytoplasmic shuttling (Bologna et al., 2018). During miRNA biogenesis, miRNAs are loaded onto AGO1 in the nucleus and exported into the cytoplasm as miRISCs

(Bologna et al., 2018). Some siRNAs, such tasiRNAs, are produced and loaded onto AGO1 in the cytosol (Bologna et al., 2018). We rationalize that mobile miRNAs are the fractions that escape AGO1 loading in the nucleus and enter the cytosol. Given the presence of cytoplasmic AGO1, the miRNAs must avoid being loaded onto AGO1 in the cytoplasm to exit the cell. Our studies with cytoplasmically sequestered AGO1 indicate that miR165/6 can be loaded onto AGO1 in the cytoplasm and disruption of MTs enhances this loading. Thus, we propose that cytoplasmic miRISC formation needs to be suppressed in source cells to enable miRNA's cell-to-cell movement and MTs play a role in this process (Figure S7). In fact, during transit, cytoplasmic RISC formation would limit the range of miRNA's cell-to-cell movement, which is consistent with the observation that expression of *KTN1* in the protoxylem partially rescues the *ktn1* mutant phenotypes. How MTs suppress the cytoplasmic loading of miRNAs is unknown. Microtubules may regulate the association of miR165/6 with AGO1 through modulating the function of chaperones, such as SQN and HSP, which play an essential role in RISC formation and AGO1 function (Du et al., 2020). Another possibility is that a fraction of AGO1 proteins normally associates with/dissociates from MTs in a dynamic manner, and the dissociation is attenuated when MTs are disrupted. If this is the case, a direct role of MTs in regulating the cytoplasmic loading of miRNAs is possible.

*KTN1* was shown to be required for miRNA-mediated translational repression in plants (Brodersen et al., 2008). In this study, we uncovered a role of *KTN1* in promoting the intercellular movement of miRNAs. Intriguingly, in the *ktn1-20* mutant, the target of amiR-SUL was derepressed at the protein but not mRNA level, consistent with the requirement of *KTN1* for amiRSUL's translation repression activity. Are the functions of *KTN1* in mediating translation repression by miRNAs and promoting the intercellular movement of miRNAs related or independent? The answer awaits future research.

### Limitations of the study

In this study, we show that dynamic and ordered microtubule organization regulated by KTN1 promotes the cell-to-cell movement of miRNAs by inhibiting their loading onto AGO1 in source cells and that this effect of microtubules on AGO1's loading of mobile miRNAs is likely exerted in the cytoplasm. However, the mechanism whereby microtubules regulate cytoplasmic AGO1 loading of miRNAs is unknown. Microtubules may regulate the subcellular localization of miRNAs or AGO1 in the cytoplasm. Through confocal microscopy and cell fractionation analysis, we did not find changes in the subcellular localization of AGO1 or miRNAs in the *ktn1* mutant. Super resolution microscopy or other high-resolution methods will be required for deciphering whether microtubules affect the distribution of miRNAs or AGO1 in the cytoplasm.

## STAR★METHODS

### RESOURCE AVAILABILITY

**Lead contact—**Further information and requests for resources and reagents should be directed to and will be fulfilled by the Lead Contact, Xuemei Chen (xuemei.chen@ucr.edu).

**Materials availability—**All reagents generated in this study are available on request from the lead contact.

### Data and code availability

- The small RNA-seq data reported in this study have been deposited in the NCBI Gene Expression Omnibus under the accession number GSE168805 and are publicly available. All data reported in this paper will be shared by the lead contact upon request.
- This paper does not report original code.
- Any additional information required to reanalyze the data reported in this paper is available from the lead contact upon request.

## EXPERIMENTAL MODEL AND SUBJECT DETAILS

*Arabidopsis thaliana* strains used in this study were all in the Columbia-0 (Col-0) background. Seeds were sterilized and grown on half-strength MS medium (PH 5.7) under long-day conditions (16 h light/8 h dark). The *SUC2::amiR-SUL* line was from Detlef Weigel (Max Planck Institute for Developmental Biology, Tubingen, Germany) (de Felippes et al., 2011). *ktn1-20* was a new allele isolated from an EMS mutagenesis screen in the *SUC2::amiR-SUL* background. *ktn1–2* (SAIL343_D12) is a T-DNA insertion mutant. Transgenic lines of *PHB::PHB-GFP, pMIR165A::GFPer, pMIR165B::GFPer, pMIR166A::GFPer, pMIR166B::GFPer* and the plasmid of *CRE1::MIR165A* were described (Miyashima et al., 2011). *UBQ10::mScarlet_MAP4* was a gift from Drs. Jingzhe Guo and Zhenbiao Yang (Pan et al., 2020).

## METHODS DETAILS

**Mutagenesis and screening—**Seeds of a homozygous *amiR* transgenic line were subjected to ethyl methanesulfonate mutagenesis as described (Jia et al., 2017; Zhang et al., 2020). The *ktn1-20* mutant was isolated based on its weaker leaf bleaching phenotype. The genomic sequence containing the coding region of *KTN1* was amplified by PCR with primers KTN1-seq-F and KTN1-seq-R and the PCR product was subjected to sequencing to identify the mutation. See Table S1 for sequences of oligonucleotides.

**Plasmid construction and plant transformation—**All constructs were made in a modified pCambia1300 vector, which contains the 35S promoter inserted between the *Eco*RI and *Sac*I sites and the NOS terminator inserted between the *Pst*I and *Hind*III sites. For genetic complementation, a genomic fragment of *KTN1*, which contains the promoter and coding regions, were amplified from *Arabidopsis* genomic DNA using primers KTN1g-F and KTN1g-R and recombined into the modified pCambia1300 that was digested with *Eco*RI and *Sal*I to remove the 35S promoter. To create plasmids for root cell-layer-specific expression of *GFP-AGO1*, *EN7* and *ACL5* promoters were amplified using primers EN7-F/EN7R and ACL5-F/ACL5-R, respectively, from *Arabidopsis* genomic DNA and inserted into pCambia1300 to replace the 35S promoter, resulting in pCambia1300-EN7 and pCambia1300ACL5, respectively, and then *GFP* and *AGO1* genomic fragments were PCR-amplified with primers GFP-F/GFP-R and AGO1-F/AGO1-R, respectively, and

recombined downstream of the *EN7* and *ACL5* promoters. Constructs for root layer-specific *KTN1* expression were obtained by inserting *EN7*, *ACL5*, *AHP6* and *SHR* promoters into pCambia1300 and then cloning the genomic fragment containing the coding region of *KTN1* downstream of the root layer-specific promoter. The primers for *EN7*, *ACL5*, *AHP6*, *SHR*, and *KTN1* PCR were EN7-F/EN7-R, ACL5-F/ACL5-R, AHP6-F/AHP6-R, SHR-F/SHR-R, and KTN1-coding-F/KTN1g-R, respectively. To construct *35S::GR-GFP-AGO1*, the ligand binding domain of *GR* was PCR-amplified from the *pGreenWUS-GR* plasmid (a gift from Venugopala (Reddy) Gonehal) (Yadav et al., 2010) using primers GR-F and GR-R and inserted into pCambia1300. *GFP* and an *AGO1* genomic fragment were PCR-amplified with primers GFP-F/GFP-R(GR) and AGO1-F(GR)/AGO1-R(GR), respectively, and fused with GR. *AGO1::GFP-AGO1* was constructed as follows. A genomic fragment containing the *AGO1* promoter was PCR-amplified using the primer pair AGO1p-F/AGO1p-R and inserted into pCambia1300 and then *GFP* and *AGO1* were PCR-amplified using primers pairs GFP-F/GFP-R and AGO1-F/AGO1-R, respectively and inserted downstream of the *AGO1* promoter. *35S::MIR165A* was constructed by inserting a 300 bp genomic fragment containing the pri-miR165A region (amplified by PCR with primers MIR165A-F and MIR-165A-R) downstream of the 35S promoter in pCambia1300. All constructs were introduced into *Agrobacterium tumefaciens* (*A. tumefaciens*) by electroporation. Stable transgenic plants were produced through *Agrobacterium tumefaciens*-mediated floral dip transformation (Clough and Bent, 1998). Transformants were selected on antibiotic medium and T2 plants with 3:1 segregation ratio of antibiotic resistance were selected and followed to the T3 generation. Homozygous plants in the T3 generation were used for experiments.

**Quantification of the leaf bleaching phenotype—**Color images of individual leaves were obtained with an Epson scanner. Image analyses were carried out in Python 3.6.5 using the open-source Open CV package (Bradski and Kaehler, 2000). Leaves were segmented from the background using a color threshold in the L*a*b* color space. From the thresholded images, binary masks were produced for each leaf. A mean blur with a kernal size of 3×3 was applied to each leaf to remove noise. The area of bleached veins was determined using an adaptive Gaussian threshold with a block size of 101 pixels. Binary masks of the bleached vein area were produced for each leaf. Binary masks for the inter-vein regions were calculated by subtracting the vein masks from the leaf masks. Leaf area, vein area and intervein area were calculated by summing the pixel values of the respective binary masks. To quantify the extent of bleaching, color images were transformed from RGB to HSV (hue, saturation, value) and the hue channel was extracted. Hue values range from 0 to 360 with yellow having a value of 60 and green having a value of 120. The mean values for the entire leaf, bleached vein area and inter-vein area were calculated with the NumPy package (Oliphant, 2006) using the respective binary masks for the original image. All values were written to a single csv file for further analysis.

**Epidermal, mesophyll and vascular tissue separation—**The separation of epidermal, mesophyll and vascular tissues was performed according to the Meselect method (Svozil et al., 2016). Briefly, three-week-old rosette leaves were placed between two tape strips. After gently peeling off the two tapes, the epidermal tissues on the abaxial side of the leaves were separated from the vascular tissue and the adaxial side of the leaves. The

tapes with the abaxial epidermis were incubated in protoplasting solution (1% cellulase Onozuka R10 (Yakult), 0.25% Maceroenzyme R10 (Yakult), 0.4 M mannitol, 10 mM $CaCl_2$, 20 mM KCl, 0.1% bovine serum albumin, 20 mM MES (PH5.7)) for 15 min at room temperature on a shaker at 50 rpm to remove the residual mesophyll cells and then washed twice with washing buffer (154 mM NaCl, 125 mM $CaCl_2$, 5 mM KCl, 2 mM MES, pH 5.7). The tapes with the abaxial epidermis were collected as epidermal tissue. The other tapes with the remaining leaf tissues were incubated in protoplasting solution for 45 min. The enzyme solution containing mesophyll cells was collected and centrifuged at 100g for 5 min at 4 °C. The pellet was washed twice with washing buffer and collected as mesophyll cells. The vascular tissue was removed from the tapes using forceps and washed twice with washing buffer. The epidermal tapes, mesophyll cells and vascular tissue were frozen in liquid nitrogen and store at −80°C before RNA extraction.

**Quantitative RT-PCR—**Total RNA was treated with DNase I (Sigma) at 37°C for 1 hour and reverse transcription was performed with RevertAid Reverse Transcriptase (ThermoFisher Scientific) using an oligo(dT) primer. Quantitative PCR was performed on the BioRad CFX96 system with SYBRGreen Supermix (BioRad). Relative expression levels were calculated using the pcr package in R (Ahmed and Kim, 2018). The *UBQ5* transcript was detected in parallel and used for normalization. The primers used are listed in Table S1.

**Grafting—**Grafting was performed according to the method described (Marsch-Martínez et al., 2013). Briefly, plants were grown vertically on ½ MS medium under short-day conditions (8 h light/16 h dark). 7day-old seedlings were used for grafting. Seedlings were placed on a thin layer of 1% agarose and cotyledons were removed from the scion. Hypocotyls were cut in the middle and scions and root stocks were aligned under a binocular stereoscope. The grafted plants were transferred back to the short-day growth chamber and incubated vertically for another 10 days. Shoots and roots were collected separately from 20–30 seedlings and subjected to RNA extraction using TRI reagent.

**Microscopy and imaging—**For xylem phenotype analysis, 5-day-old seedlings were stained in 0.0001% basic fuchsin in 95% ethanol for 5 min, and then washed two times with 70% ethanol (Smith et al., 2013). Primary roots were cut and mounted in 50% glycerol, and observed under an Olympus BX53 fluorescence microscope. To quantify the distribution pattern of PHB-GFP, 10–15 individual roots were imaged by Z-stack scanning under confocal laser-scanning microscopy (CLSM) PHB-GFP fluorescent signals were quantified on the Z-projection (sum slices) from 10 images that span 40 μm across the root diameter. A 50 μm X 10 μm rectangular region located approximately 80 μm above the QC was selected (care was exercised to ensure the inclusion of nuclei in the rectangle), and fluorescent signals in this region were quantified using the ImageJ software (NIH). The PHB-GFP gradient was also measured by selecting individual nuclei in the center-most cell file and corresponding nuclei in the neighboring cell file. The ratios of the pairs of nuclei (nucleus in the neighboring cell file vs. nucleus in the center-most cell file) were calculated to represent the distribution of PHB-GFP. A region without PHB-GFP signals was selected as background, the fluorescence signals of which were subtracted from those of measured areas or nuclei. CLSM was performed on Leica SP5 and Zeiss LSM 780 microscopes. Roots

were stained with 10 μM propidium iodide followed by CLSM. GFP was excited at 488 nm and emission was detected at 500–520 nm. Propidium iodide was excited at 488 nm and emission was detected at 600–650 nm. DAPI was excited at 405 nm and emission was detected at 430–480 nm.

Cytoplasmic streaming analysis was conducted with bright field microscopy (Leica SP5). The velocity of cytoplasmic streaming was measured by tracking the movement of visible cytoplasmic particles undergoing continuous movement for at least 5 s using the ImageJ software (NIH).

**In situ hybridization—**In situ hybridization was performed as described (Javelle and Timmermans, 2012). An LNA probe with complementary sequence to miR166 was synthesized and double digoxigenin labeled at Qiagen. An LNA probe with sequence complementary to mouse miR124 was used as the negative control.

**Nuclear-cytoplasmic fractionation—**12-day-old seedlings were ground into fine powder in liquid nitrogen and the powder was resuspended with lysis buffer (20 mM Tris-HCl at PH 7.5, 20 mM KCl, 2 mM EDTA, 2.5 mM $MgCl_2$, 25% glycerol, 250 mM Sucrose, 5 mM DTT and protease inhibitor cocktail (Roche)) at 2ml/g. The suspension was filtered through double layers of Miracloth and centrifuged at 1500g for 15 min.The supernatant was transferred into a new tube and centrifuged at 10,000g for 10 min at 4 °C.The supernatant was collected as the cytoplasmic fraction. The pellet was then washed six times with nuclear resuspension buffer (NRB: 20 mM Tris-HCl, pH 7.4, 25% glycerol, 2.5 mM $MgCl_2$, and 0.2% Triton X-100). The pellet was then resuspended with 500 μl NRB2 (20 mM Tris-HCl, pH 7.5, 0.25 M sucrose, 10 mM $MgCl_2$, 0.5% Triton X-100, and 5 mM 2-mercaptoethanol) and the suspension was carefully laid on top of 500 μl NRB3 (20 mM Tris-HCl, pH7.5, 10 mM $MgCl_2$, 1.7 M sucrose, 0.5% Triton X-100, 5 mM 2-mercaptoethanol and protease inhibitor cocktail (Roche). The samples were centrifuged at 16,000g for 45 min at 4°C. The pellet was collected as the nuclear fraction. 10% of the cytoplasmic and nuclear fractions were boiled in 1 X SDS sample loading buffer (50 mM Tris-Cl at pH 6.8, 2% SDS, 0.1% bromophenol blue, 10% glycerol, 1% 2mercaptoethanol) and saved for protein gel blot analysis. The remaining cytoplasmic and nuclear fractions were subjected to RNA extraction using TRI reagent.

**RNA gel blot analysis of small RNAs—**12-day-old seedlings were ground into powder in liquid nitrogen and RNA was extracted using the TRI reagent (Molecular Research Center, Inc) according to the manufacturer's instructions. Small RNA gel blot analysis was performed as described (Li et al., 2016). 5 μg total RNA from Col and *ktn1-20* was resolved on 15% Urea-PAGE gels and transferred onto Hybond NX membranes (GE Healthcare Life Sciences) followed by chemical cross-linking using EDC (1ethyl-3-(3-dimethylaminopropyl) carbodiimide hydrochloride). Complementary oligonucleotides were end-labeled with $^{32}P$ and used to probe the membrane. The bands on the RNA gel blot were quantified by ImageQuant TL 8.1 and normalized against U6 or tRNA. The oligonucleotide probes used are listed in Table S1.

**Immunoprecipitation of root layer-specific GFP-AGO1—**9-day-old *Arabidopsis* roots of *EN7::GFP-AGO1* and *ACL5::GFP-AGO1* transgenic lines in WT and *ktn1-20* backgrounds were collected and ground into powder in liquid nitrogen. Cells were lysed in immunoprecipitation buffer (50 mM Tris 7.5, 150 mM NaCl, 4 mM $MgCl_2$, 2 mM DTT, 10% Glycerol, 0.1% NP-40, 1x proteinase inhibitor cocktail (Roche)) by gentle rotation at 4°C for 30 min. Cell debris was removed by centrifugation twice at 15000 rpm for 20 min at 4 °C. The supernatant was incubated with GFP-Trap_MA (ChromoTek) for 2 h with gentle rotation. The beads were washed 5 times with washing buffer (50 mM Tris 7.5, 150 mM NaCl, 4 mM $MgCl_2$, 2 mM DTT, 10% Glycerol, 0.5% NP-40, 1x proteinase inhibitor cocktail (Roche). Beads were magnetically collected and 10% GFP-AGO1 immunoprecipitates were boiled in 1X SDS sample loading buffer for protein gel blot analysis and the remainder was subjected to RNA extraction using the TRI reagent.

**Protein gel blot analysis—**Total proteins from twelve-day-old seedlings were resolved by SDS-PAGE, transferred to nitrocellulose membranes, blocked in 1X PBS + 0.05% Tween-20 supplemented with 5% non-fat milk for 1 hr and incubated with primary antibodies at 4°C overnight. After washing three times in 1X PBS + 0.05% Tween-20, membranes were incubated with horseradish peroxidase-conjugated secondary anti-bodies for 1 hour, then rinsed three times and detected with ECL western blotting detection reagent (Cytiva Amersham).

**Small RNA sequencing and data analysis—**To construct small RNA libraries from total RNA, 20 μg total RNA from 14-day-old seedlings was resolved in a 15% Urea-PAGE gel and small RNAs of 15–40 nt were isolated from the gel and subjected to small RNA library construction using NEBNext Multiplex Small RNA Library Prep Set for Illumina (E7300). Small RNAs extracted from GFP-AGO1 IP products were processed into sequencing libraries using NEBNext Multiplex Small RNA Library Prep Set for Illumina (E7300) without fractionation by gel electrophoresis. The libraries were sequenced on an Illumina HiSeq 2500. sRNA-seq data were analyzed using the pRNASeqTools pipeline (https://github.com/grubbybio/pRNASeqTools). Raw reads from sRNA-seq were first trimmed to remove the adaptor sequence (AGATCGGAAGAGC) by cutadapt 3.0. The trimmed reads were mapped to the *Arabidopsis* genome (Araport 11) using Shortstack 3.4 with parameter "'-bowtie_m 1000 --ranmax 50 --mmap u --mismatches 0". The miRNA levels were quantified by calculating the RPM (reads per million mapped reads). Two biological replicates for each genotype were included.

**Transient expression of GR-GFP-AGO1 and IP in *N. benthamiana*—**Transient expression in *N. benthamiana* was performed as described (Martin et al., 2009). The *A. tumefaciens* strain GV3101 carrying *35S::MIR165A*, *35S::GR-GFP-AGO1* and *UBQ10::mScarletMAP4* were infiltrated into the leaves of three-week-old *N. benthamiana*. At 36 hours post infiltration, the leaves were infiltrated with 20 μM oryzalin (Sigma) or 0.02% DMSO (mock treatment). Leaves were collected at 24 hours post oryzalin or mock infiltration. IP was performed using GFP-Trap_MA (ChromoTek) as described above. The imaging of GR-GFP-AGO1 and mScarlet-MAP4 was performed using CLSM as described above. 5 μg/ml DAPI was used to stain the nuclei.

## Supplementary Material

Refer to Web version on PubMed Central for supplementary material.

## ACKNOWLEDGMENTS

We thank Chenjiang You and Brandon H. Le for training Lusheng Fan in data analysis. We are grateful to Drs. Detlef Weigel, Zhenbiao Yang and Venugopala (Reddy) Gonehal for sharing the *SUC2::amiR-SUL* transgenic line, the *UBQ10::mScarlet_MAP4* plasmid and the *pGreen-WUSGR* plasmid, respectively. We thank Brandon H. Le for comments on the manuscript. This work was supported by National Institutes of Health (GM129373) to X.C.

## REFERENCES

Ahmed M, and Kim DR (2018). pcr: an R package for quality assessment, analysis and testing of qPCR data. PeerJ 6, e4473. [PubMed: 29576953]

Baumberger N, and Baulcombe D (2005). *Arabidopsis* ARGONAUTE1 is an RNA Slicer that selectively recruits microRNAs and short interfering RNAs. Proc. Natl. Acad. of Sci 102, 1192811933.

Bologna NG, Iselin R, Abriata LA, Sarazin A, Pumplin N, Jay F, Grentzinger T, Dal Peraro M, and Voinnet O (2018). Nucleo-cytosolic shuttling of ARGONAUTE1 prompts a revised model of the plant microRNA pathway. Molecular Cell 69, 709–719 e705. [PubMed: 29398448]

Bologna NG, and Voinnet O (2014). The diversity, biogenesis, and activities of endogenous silencing small RNAs in *Arabidopsis*. Annu. Rev. Plant Biol 65, 473–503. [PubMed: 24579988]

Boyko V, Hu Q, Seemanpillai M, Ashby J, and Heinlein M (2007). Validation of microtubuleassociated Tobacco mosaic virus RNA movement and involvement of microtubule-aligned particle trafficking. Plant J. 51, 589–603. [PubMed: 17584190]

Bradski G, and Kaehler A (2000). OpenCV. Dr. Dobb's journal of software tools 3.

Brodersen P, Sakvarelidze-Achard L, Bruun-Rasmussen M, Dunoyer P, Yamamoto YY, Sieburth L, and Voinnet O (2008). Widespread translational inhibition by plant miRNAs and siRNAs. Science 320, 1185–1190. [PubMed: 18483398]

Brosnan CA, Sarazin A, Lim P, Bologna NG, Hirsch-Hoffmann M, and Voinnet O (2019). Genome-scale, single-cell-type resolution of microRNA activities within a whole plant organ. EMBO J. 38, e100754. [PubMed: 31268601]

Buhtz A, Pieritz J, Springer F, and Kehr J (2010). Phloem small RNAs, nutrient stress responses, and systemic mobility. BMC Plant Biol. 10, 1–13. [PubMed: 20047654]

Carlsbecker A, Lee JY, Roberts CJ, Dettmer J, Lehesranta S, Zhou J, Lindgren O, Moreno-Risueno MA, Vaten A, Thitamadee S, et al. (2010). Cell signalling by microRNA165/6 directs gene dose-dependent root cell fate. Nature 465, 316–321. [PubMed: 20410882]

Chen X, and Rechavi O (2022). Plant and animal small RNA communications between cells and organisms. Nat. Rev. Mol. Cell Biol 23, 185–203. [PubMed: 34707241]

Chitwood DH, Nogueira FT, Howell MD, Montgomery TA, Carrington JC, and Timmermans MC (2009). Pattern formation via small RNA mobility. Genes Dev. 23, 549–554. [PubMed: 19270155]

Clough SJ, and Bent AF (1998). Floral dip: a simplified method for Agrobacterium-mediated transformation of *Arabidopsis thaliana*. Plant J. 16, 735–743. [PubMed: 10069079]

Dalmadi Á, Gyula P, Bálint J, Szittya G, and Havelda Z (2019). AGO-unbound cytosolic pool of mature miRNAs in plant cells reveals a novel regulatory step at AGO1 loading. Nuc. Acid. Res 47, 9803–9817.

de Felippes FF, Ott F, and Weigel D (2011). Comparative analysis of non-autonomous effects of tasiRNAs and miRNAs in *Arabidopsis thaliana*. Nuc. Acid. Res 39, 2880–2889.

Devers EA, Brosnan CA, Sarazin A, Albertini D, Amsler AC, Brioudes F, Jullien PE, Lim P, Schott G, and Voinnet O (2020). Movement and differential consumption of short interfering RNA duplexes underlie mobile RNA interference. Nat. Plants 6, 789–799 [PubMed: 32632272]

Dittmar KD, Demady DR, Stancato LF, Krishna P, and Pratt WB (1997). Folding of the glucocorticoid receptor by the heat shock protein (hsp) 90-based chaperone machinery: The role of p23 is to

stabilize receptor· hsp90 heterocomplexes formed by hsp90· p60· hsp70. J.of Biol. Chem 272, 21213–21220. [PubMed: 9261129]

Du F, Gong W, Bosca S, Tucker M, Vaucheret H, and Laux T (2020). Dose-dependent AGO1-mediated inhibition of the miRNA165/166 pathway modulates stem cell maintenance in *Arabidopsis* shoot apical meristem. Plant commun. 1, 100002. [PubMed: 33404539]

Ehrhardt DW, and Shaw SL (2006). Microtubule dynamics and organization in the plant cortical array. Annu. Rev. Plant Biol 57, 859–875. [PubMed: 16669785]

Heidstra R, Welch D, and Scheres B (2004). Mosaic analyses using marked activation and deletion clones dissect *Arabidopsis* SCARECROW action in asymmetric cell division. Genes Dev 18, 1964–1969. [PubMed: 15314023]

Horstman A, Li M, Heidmann I, Weemen M, Chen B, Muino JM, Angenent GC, and Boutilier K (2017). The BABY BOOM transcription factor activates the LEC1-ABI3-FUS3-LEC2 network to induce somatic embryogenesis. Plant Phys. 175, 848–857.

Javelle M, and Timmermans MC (2012). In situ localization of small RNAs in plants by using LNA probes. Nat. Prot 7, 533–541.

Jia T, Zhang B, You C, Zhang Y, Zeng L, Li S, Johnson KCM, Yu B, Li X, and Chen X (2017). The *Arabidopsis* MOS4-associated complex promotes microRNA biogenesis and precursor messenger RNA splicing. Plant Cell 29, 2626–2643. [PubMed: 28947490]

Kawamura E, and Wasteneys GO (2008). MOR1, the *Arabidopsis thaliana* homologue of Xenopus MAP215, promotes rapid growth and shrinkage, and suppresses the pausing of microtubules *in vivo*. J. Cell Sci121, 4114–4123. [PubMed: 19033380]

Klesen S, Hill K, and Timmermans MC (2020). Small RNAs as plant morphogens. Curr. Topics Dev. Biol 137, 455–480.

Knauer S, Holt AL, Rubio-Somoza I, Tucker EJ, Hinze A, Pisch M, Javelle M, Timmermans MC, Tucker MR, and Laux T (2013). A protodermal miR394 signal defines a region of stem cell competence in the *Arabidopsis* shoot meristem. Dev. Dell 24, 125–132.

Lewsey MG, Hardcastle TJ, Melnyk CW, Molnar A, Valli A, Urich MA, Nery JR, Baulcombe DC, and Ecker JR (2016). Mobile small RNAs regulate genome-wide DNA methylation. Proc. Natl. Acad. Sci 113, E801–E810. [PubMed: 26787884]

Li S, Le B, Ma X, Li S, You C, Yu Y, Zhang B, Liu L, Gao L, and Shi T (2016). Biogenesis of phased siRNAs on membrane-bound polysomes in *Arabidopsis*. Elife 5, e22750. [PubMed: 27938667]

Li S, Liu L, Zhuang X, Yu Y, Liu X, Cui X, Ji L, Pan Z, Cao X, Mo B, et al. (2013). MicroRNAs inhibit the translation of target mRNAs on the endoplasmic reticulum in *Arabidopsis*. Cell 153, 562–574. [PubMed: 23622241]

Li S, Wang X, Xu W, Liu T, Cai C, Chen L, Clark CB, and Ma J (2021). Unidirectional movement of small RNAs from shoots to roots in interspecific heterografts. Nat. Plants 7, 50–59. [PubMed: 33452489]

Lin D, Cao L, Zhou Z, Zhu L, Ehrhardt D, Yang Z, and Fu Y (2013). Rho GTPase signaling activates microtubule severing to promote microtubule ordering in *Arabidopsis*. Curr. Biol 23, 290–297. [PubMed: 23394835]

Lin S-I, Chiang S-F, Lin W-Y, Chen J-W, Tseng C-Y, Wu P-C, and Chiou T-J (2008). Regulatory network of microRNA399 and PHO2 by systemic signaling. Plant Phys. 147, 732–746.

Marsch-Martínez N, Franken J, Gonzalez-Aguilera KL, de Folter S, Angenent G, and Alvarez-Buylla ER (2013). An efficient flat-surface collar-free grafting method for *Arabidopsis thaliana* seedlings. Plant Methods 9, 1–9. [PubMed: 23286457]

Martin K, Kopperud K, Chakrabarty R, Banerjee R, Brooks R, and Goodin MM (2009). Transient expression in *Nicotiana benthamiana* fluorescent marker lines provides enhanced definition of protein localization, movement and interactions in planta. Plant J. 59, 150–162. [PubMed: 19309457]

Melnyk CW, Molnar A, Bassett A, and Baulcombe DC (2011). Mobile 24 nt small RNAs direct transcriptional gene silencing in the root meristems of *Arabidopsis thaliana*. Curr. Biol 21, 1678–1683. [PubMed: 21962713]

Merelo P, Ram H, Caggiano MP, Ohno C, Ott F, Straub D, Graeff M, Cho SK, Yang SW, and Wenkel S (2016). Regulation of MIR165/166 by class II and class III homeodomain leucine zipper proteins establishes leaf polarity. Proc. Natl. Acad. Sci 113, 11973–11978. [PubMed: 27698117]

Miyashima S, Koi S, Hashimoto T, and Nakajima K (2011). Non-cell-autonomous microRNA165 acts in a dose-dependent manner to regulate multiple differentiation status in the *Arabidopsis* root. Development 138, 2303–2313. [PubMed: 21558378]

Molnar A, Melnyk CW, Bassett A, Hardcastle TJ, Dunn R, and Baulcombe DC (2010). Small silencing RNAs in plants are mobile and direct epigenetic modification in recipient cells. Science 328, 872–875. [PubMed: 20413459]

Muniz L, Minguet EG, Singh SK, Pesquet E, Vera-Sirera F, Moreau-Courtois CL, Carbonell J, Blazquez MA, and Tuominen H (2008). ACAULIS5 controls *Arabidopsis* xylem specification through the prevention of premature cell death. Development 135, 2573–2582. [PubMed: 18599510]

Muraro D, Mellor N, Pound MP, Lucas M, Chopard J, Byrne HM, Godin C, Hodgman TC, King JR, and Pridmore TP (2014). Integration of hormonal signaling networks and mobile microRNAs is required for vascular patterning in *Arabidopsis* roots. Proc. Natl. Acad. Sci 111, 857–862. [PubMed: 24381155]

Okuma N, Soyano T, Suzaki T, and Kawaguchi M (2020). MIR2111–5 locus and shootaccumulated mature miR2111 systemically enhance nodulation depending on HAR1 in Lotus japonicus. Nat. Commun 11, 5192. [PubMed: 33060582]

Oliphant TE (2006). A guide to NumPy, Vol 1 (Trelgol Publishing USA).

Pan X, Fang L, Liu J, Senay-Aras B, Lin W, Zheng S, Zhang T, Guo J, Manor U, Van Norman J, et al. (2020). Auxin-induced signaling protein nanoclustering contributes to cell polarity formation. Nature Commun. 11, 3914. [PubMed: 32764676]

Pant BD, Buhtz A, Kehr J, and Scheible WR (2008). MicroRNA399 is a long-distance signal for the regulation of plant phosphate homeostasis. Plant J. 53, 731–738. [PubMed: 17988220]

Schneider R, Klooster K.v.t., Picard KL, van der Gucht J, Demura T, Janson M, Sampathkumar A, Deinum EE, Ketelaar T, and Persson S (2021). Long-term single-cell imaging and simulations of microtubules reveal principles behind wall patterning during protoxylem development. Nat. Commun 12, 669 [PubMed: 33510146]

Skopelitis DS, Benkovics AH, Husbands AY, and Timmermans MCP (2017). Boundary formation through a direct threshold-based readout of mobile small RNA gradients. Dev. Cell 43, 265–273 e266. [PubMed: 29107557]

Skopelitis DS, Hill K, Klesen S, Marco CF, von Born P, Chitwood DH, and Timmermans MCP (2018). Gating of miRNA movement at defined cell-cell interfaces governs their impact as positional signals. Nat. Commun 9, 3107. [PubMed: 30082703]

Smith RA, Schuetz M, Roach M, Mansfield SD, Ellis B, and Samuels L (2013). Neighboring parenchyma cells contribute to *Arabidopsis* xylem lignification, while lignification of interfascicular fibers is cell autonomous. Plant Cell 25, 3988–3999. [PubMed: 24096341]

Svozil J, Gruissem W, and Baerenfaller K (2016). Meselect - A Rapid and Effective Method for the Separation of the Main Leaf Tissue Types. Front.Plant Sci 7, 1701. [PubMed: 27895656]

Vaten A, Dettmer J, Wu S, Stierhof YD, Miyashima S, Yadav SR, Roberts CJ, Campilho A, Bulone V, Lichtenberger R, et al. (2011). Callose biosynthesis regulates symplastic trafficking during root development. Dev. Cell 21, 1144–1155. [PubMed: 22172675]

Webb M, Jouannic S, Foreman J, Linstead P, and Dolan L (2002). Cell specification in the *Arabidopsis* root epidermis requires the activity of ECTOPIC ROOT HAIR 3–a katanin-p60 protein. Development 129, 123–131. [PubMed: 11782406]

Whittington AT, Vugrek O, Wei KJ, Hasenbein NG, Sugimoto K, Rashbrooke MC, and Wasteneys GO (2001). MOR1 is essential for organizing cortical microtubules in plants. Nature 411, 610–613. [PubMed: 11385579]

Yadav RK, Tavakkoli M, and Reddy GV (2010). WUSCHEL mediates stem cell homeostasis by regulating stem cell number and patterns of cell division and differentiation of stem cell progenitors. Development 137, 3581–3589. [PubMed: 20876644]

Yu Y, Ji L, Le BH, Zhai J, Chen J, Luscher E, Gao L, Liu C, Cao X, Mo B, et al. (2017). ARGONAUTE10 promotes the degradation of miR165/6 through the SDN1 and SDN2 exonucleases in *Arabidopsis*. PLoS Biol. 15, e2001272. [PubMed: 28231321]

Yu Y, Zhang Y, Chen X, and Chen Y (2019). Plant noncoding RNAs: hidden players in development and stress responses. Annu. Rev. Cell Dev. Biol 35, 407–431. [PubMed: 31403819]

Zhang B, You C, Zhang Y, Zeng L, Hu J, Zhao M, and Chen X (2020). Linking key steps of microRNA biogenesis by TREX-2 and the nuclear pore complex in *Arabidopsis*. Nat. Plants 6, 957–969. [PubMed: 32690891]

Zhang W, Kollwig G, Stecyk E, Apelt F, Dirks R, and Kragler F (2014). Graft-transmissible movement of inverted-repeat-induced si RNA signals into flowers. Plant J. 80, 106–121. [PubMed: 25039964]

Zhao Y, Yu Y, Zhai J, Ramachandran V, Dinh TT, Meyers BC, Mo B, and Chen X (2012). The Arabidopsis nucleotidyl transferase HESO1 uridylates unmethylated small RNAs to trigger their degradation. Curr. Biol 22, 689–694. [PubMed: 22464194]

Zhu H, Hu F, Wang R, Zhou X, Sze SH, Liou LW, Barefoot A, Dickman M, and Zhang X (2011). *Arabidopsis* Argonaute10 specifically sequesters miR166/165 to regulate shoot apical meristem development. Cell 145, 242–256. [PubMed: 21496644]

**Highlights:**

- KTN1 promotes the non-cell autonomous activities of microRNAs
- KTN1 is required in the source cells for the non-cell autonomous action of miR165/6
- Microtubules promote the movement of miR165/6 by inhibiting its loading onto AGO1
- Microtubules suppress the association of miR165/6 with AGO1 in the cytoplasm

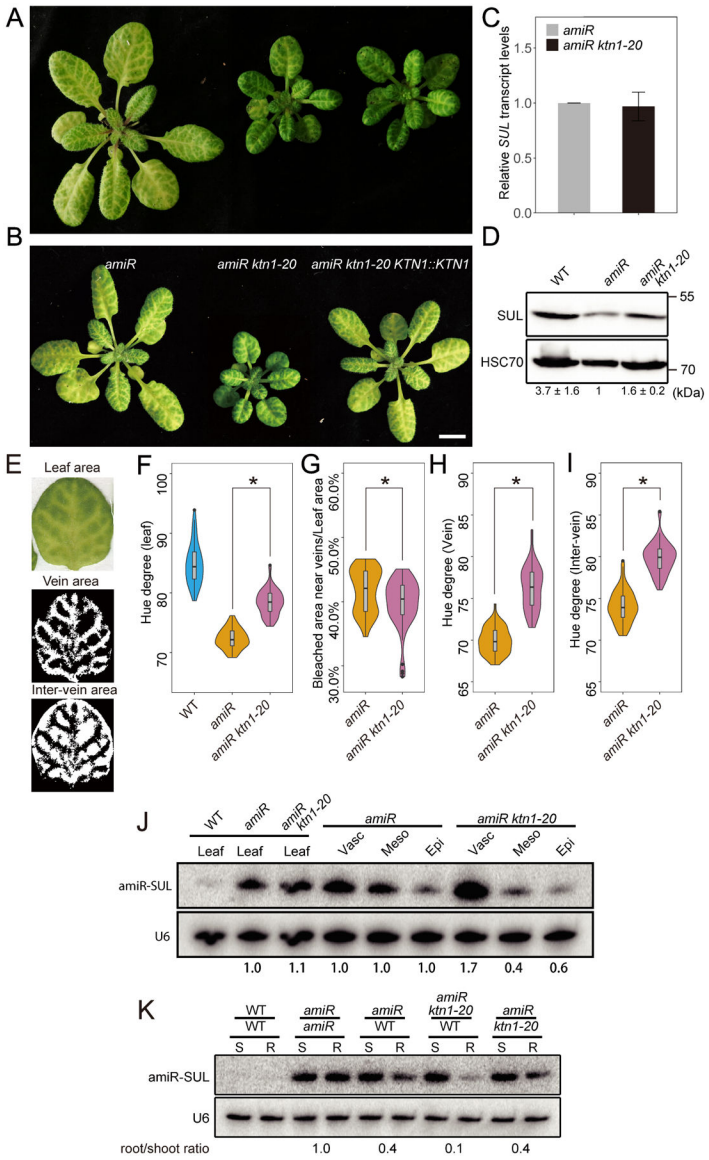


**Figure 1. *KTN1* is required for intercellular and systemic movement of amiR-SUL.**

4-week-old plants of *amiR* (*amiR*), *amiR ktn1-20* and *amiR ktn1–2*. (B) 4-week-old plants of *amiR, amiR ktn1-20 and amiR ktn1-20 KTN1::KTN1,* showing that *KTN1::KTN1* fully rescues the developmental and leaf bleaching phenotypes of *ktn1-20*. Scale bars in (A) and (B), 1 cm. (C) Relative levels of the *SUL* transcript in *amiR* and *amiR ktn1-20*. Error bars represent SD calculated from three biological replicates, each with three technical replicates. *UBQ5* RNA served as the internal control. (D) SUL protein in *amiR* and *amiR ktn1-20* as determined by protein gel blot analysis with anti-SUL antibodies. HSC70 served as the loading control. The SUL protein level was first quantified against HSC70, and then normalized to the genotype *amiR*. Relative protein levels are indicated below the gel images by numbers representing mean+/−SD calculated from three biological replicates. (E) Representative images used to quantify areas of leaf chlorosis. (F) Hue color value representing the levels of chlorosis for whole leaves in wild type (WT), *amiR* and *amiR*

*ktn1-20*. Lower values correspond to increased chlorosis. 60 degrees represent yellow and 120 degrees represent green. (G) Quantification of the area of vein-centered bleaching normalized against total leaf area in *amiR* and *amiR ktn1-20*. (H and I) Quantification of levels of chlorosis (indicated by hue value) for vein and inter-vein regions in *amiR* and *amiR ktn1-20. p*-values were calculated by Student's *t* test. *, *p*-value < 0.01. 60 leaves from 10 individual plants were analyzed for *amiR* and *amiR ktn1-20* in (F) to (I). (J) RNA gel blot analysis of amiR-SUL in Meselect-separated vascular, mesophyll and epidermal tissues. U6 was used as a loading control. The amiR-SUL levels in *amiR ktn1-20* were relative to those in *amiR* in each tissue and indicated by the numbers below the gel images. (K) RNA gel blot analysis of amiRSUL in scions (S) and rootstocks (R) of WT, *amiR*, *amiR ktn1-20*, *and ktn1-20* in the indicated grafting combinations. The values below the gel images represent root/shoot ratios of amiR-SUL relative to that of *amiR*/amiR set as 1.0. See also Figures S1 and S2.

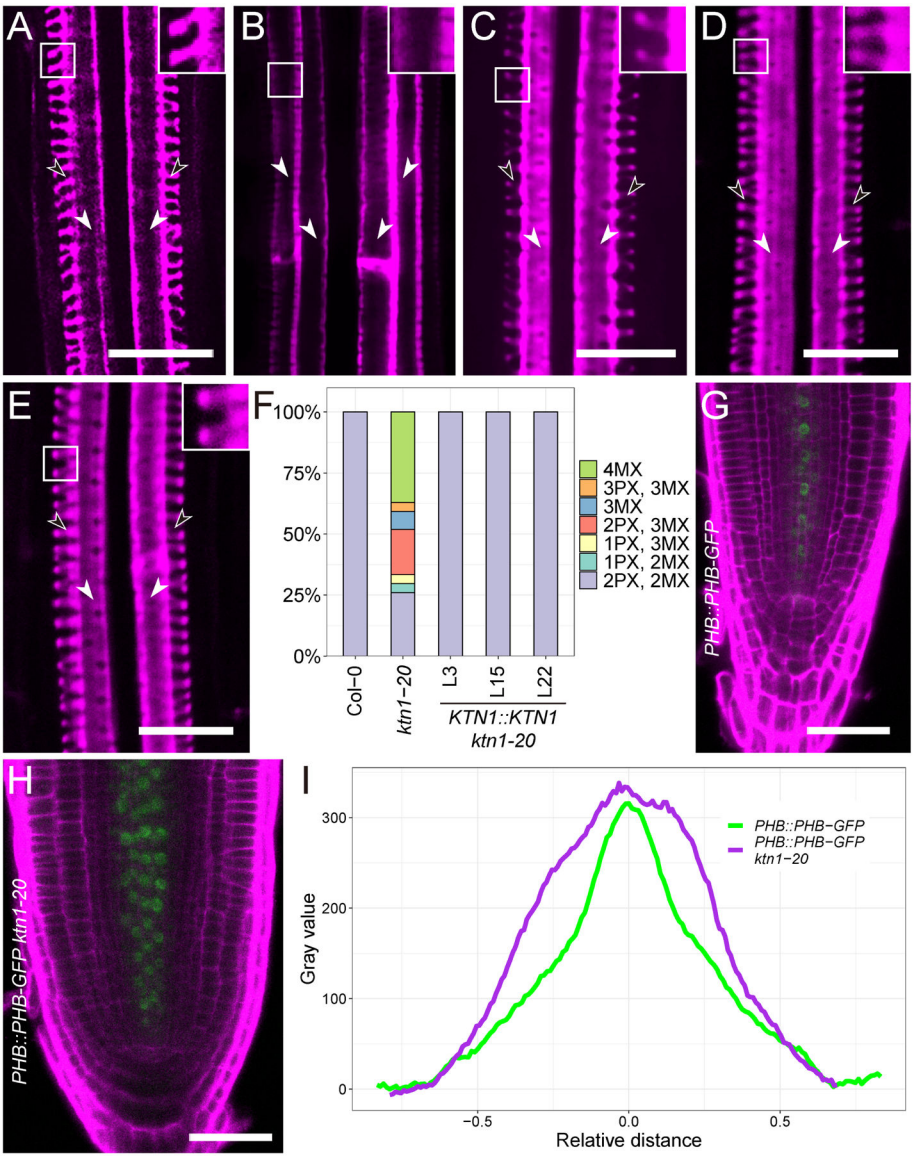


**Figure 2. Defects in xylem patterning and PHB-GFP gradient distribution in the *ktn1-20* mutant.**

(A-E) Xylem patterns in WT (A), *ktn1-20* (B) and three independent complementation lines *KTN1::KTN1 ktn1-20* (C-E). The white arrowheads indicate the two metaxylem layers flanked by two protoxylem layers (open arrowheads). In the *ktn1-20* image, four layers of metaxylem are seen. Insets, high magnification images showing the presence (A, C-E) and absence (B) of spiral cell wall thickenings. (F) Quantification of xylem phenotypes in WT (Col-0), *ktn1-20* and *KTN1::KTN1 ktn1-20*. 20–30 individual roots were analyzed. In some roots of the *ktn1-20* mutant, xylem cell wall morphology was intermediate between protoxylem and metaxylem such that the spiral cell wall thickening pattern was not as striking. Such xylem was counted as metaxylem, as an obvious cell-cell boundary was found between two consecutive cells, while such boundary is not present in protoxylem. (G) Expression patterns of *PHB::PHB-GFP* in WT (G) and *ktn1-20* (H). Scale bars, 20 μm in (A-E); 50 μm in (G) and (H). (I) Quantification of PHB-GFP signal intensity measured

across the root diameter in WT and *ktn1-20*. 10–15 individual roots were imaged for quantification. See also Figures S3 and S4.

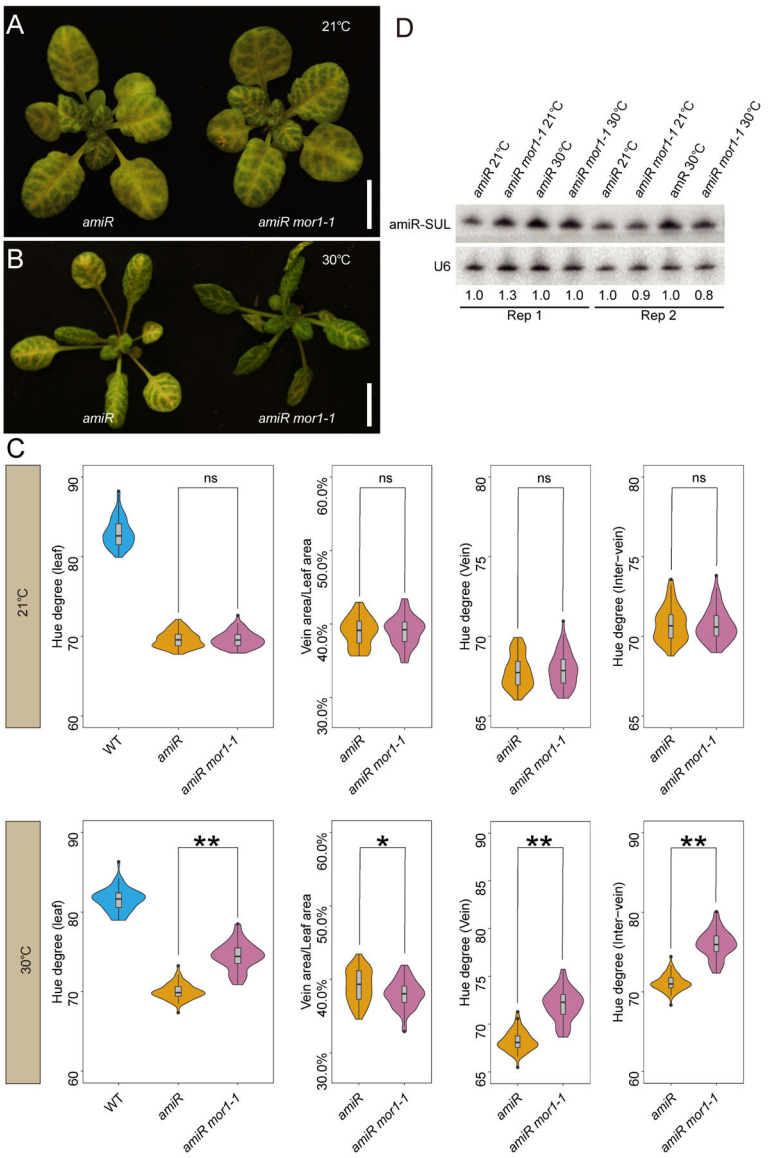


**Figure 3. The *mor1-1* mutation suppresses amiR-SUL-mediated silencing.**

(A) Three-week-old plants of *amiR* and *amiR mor1-1* grown at 21°C. No obvious differences in vein-centered bleaching between the two genotypes were observed. Scale bars, 1cm. (B) 10-dayold plants of *amiR* and *amiR mor1-1* grown at 21°C were transferred to 30°C and grown for another 10 days. *amiR mor1-1* plants exhibited weaker leaf chlorosis. Scale bars, 1cm. (C) Hue color value representing the levels of chlorosis for whole leaves, vein and inter-vein regions in wild type (WT) *amiR* and *amiR mor1-1* grown at 21°C and 30°C. Bleaching areas were represented by the ratio between vein area and whole leaf. *p*-values were calculated by Student's *t* test. *, *p*value < 0.05, **; *p*-value < 0.01; ns, not significant. (D) RNA gel blot analysis of amiR-SUL in *amiR* and *amiR mor1-1* grown under either 21°C or 30°C as described above. Relative signal intensities were normalized against U6 and values were given. Two biological replicates (Rep) were included. See also Figure S3.

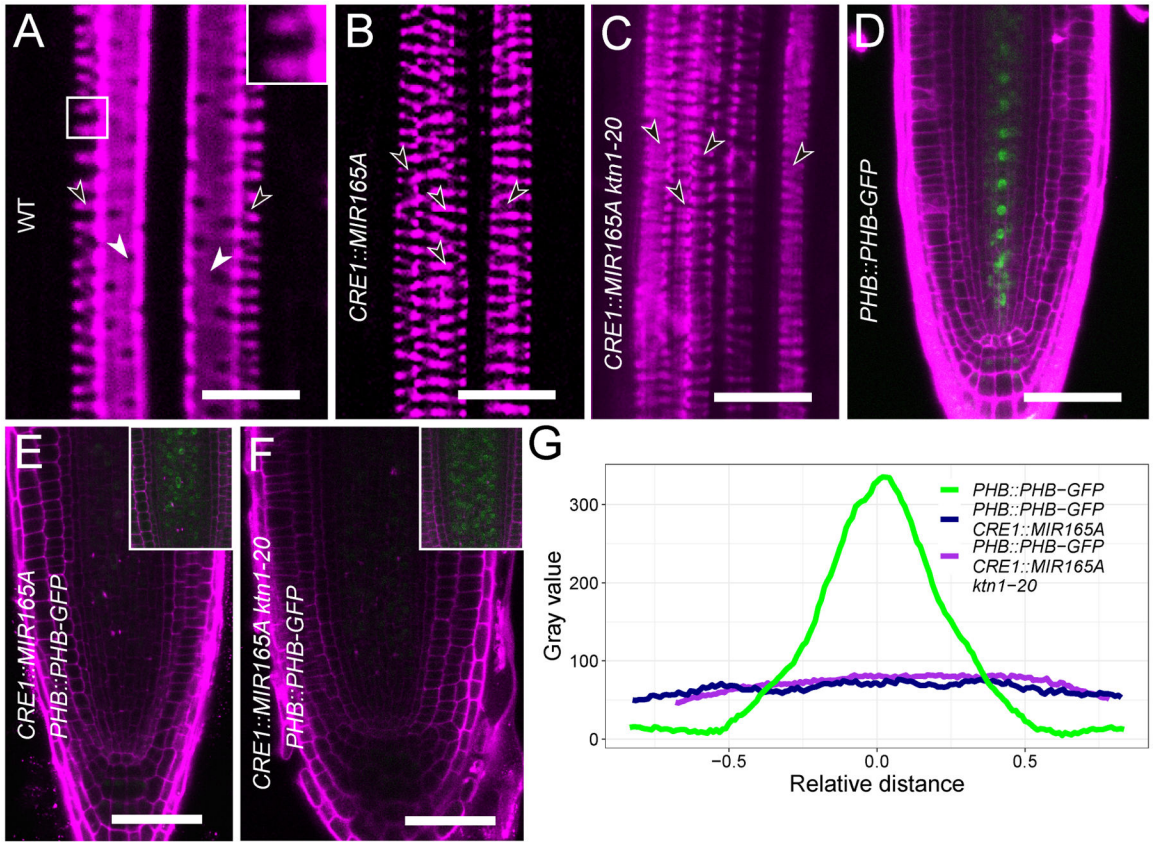


**Figure 4. *KTN1* is dispensable for the cell-autonomous activity of miR165/6.**

(A, B) Xylem patterns in WT (A), *CRE1::MIR165A* (B) and *CRE1::MIR165A ktn1-20* (C). Metaxylem-to-protoxylem transformation is seen in both genotypes. Filled arrowheads indicate metaxylem and unfilled arrowheads indicate protoxylem. (D-F) Expression patterns of *PHB-GFP* in WT (D), *pCRE1::miR165A* (E) and *pCRE1::miR165A ktn1-20* (F). Scale bars, 20 μm in (A-C); 50 μm in (D-E). Insets, high magnification images. (G) Quantification of PHB-GFP signal intensity across the root diameter in *pCRE1::miR165A* and *pCRE1::miR165A ktn1-20*. 10 individual roots were imaged for the quantification for each genotype.

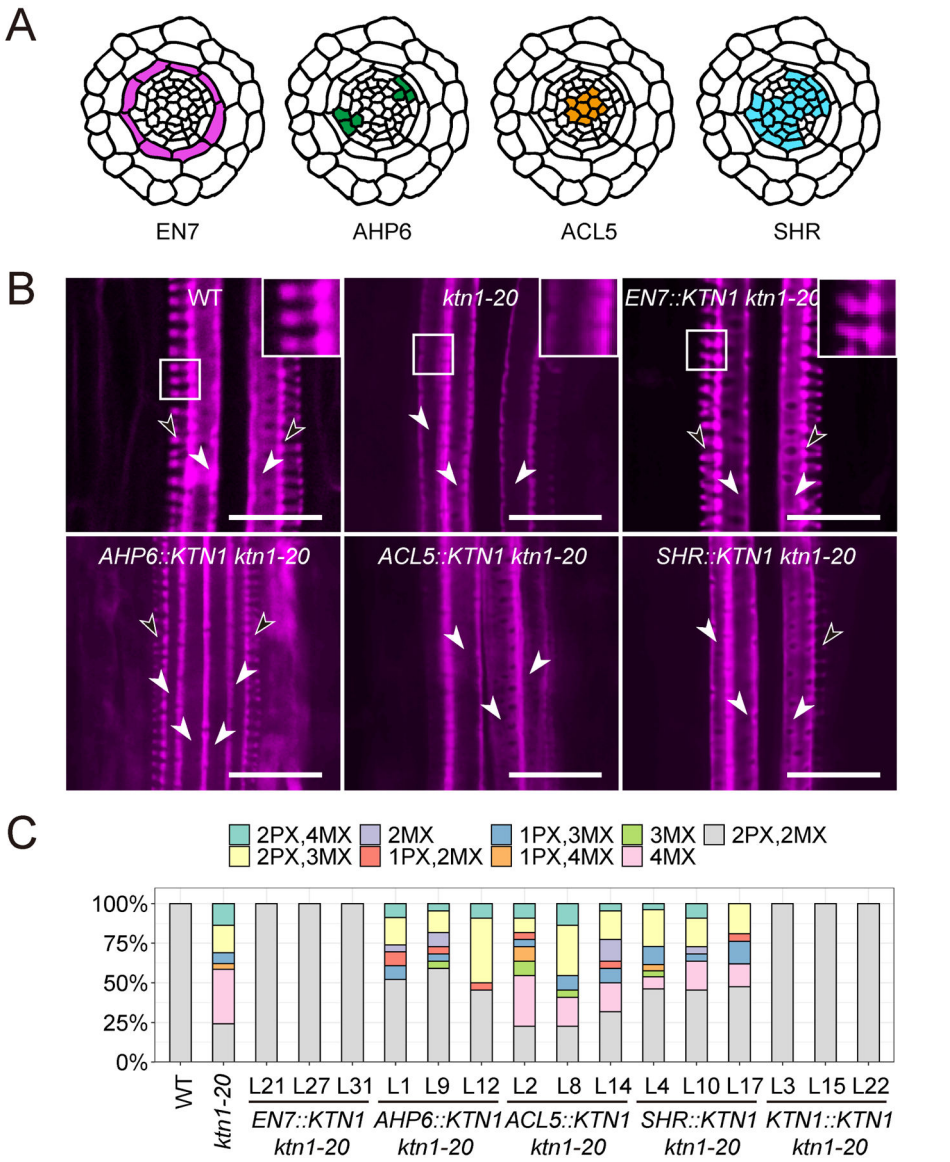


**Figure 5. Expression of *KTN1* in the endodermis is crucial for xylem pattern formation.**

(A) Schematic representation of cross sections of an *Arabidopsis* root. Cell layers relevant to the tissue-specific expression of *KTN1* are colored. (B) Representative images showing xylem patterns in the indicated genotypes. Scale bars, 20 μm. Insets show the high magnification images. Filled arrowheads indicate metaxylem and unfilled arrowheads indicate protoxylem. (C) Quantification of the xylem phenotypes in the indicated genotypes. Three independent transgenic lines were analyzed for each transgene. 20–30 individual roots were included for each genotype.

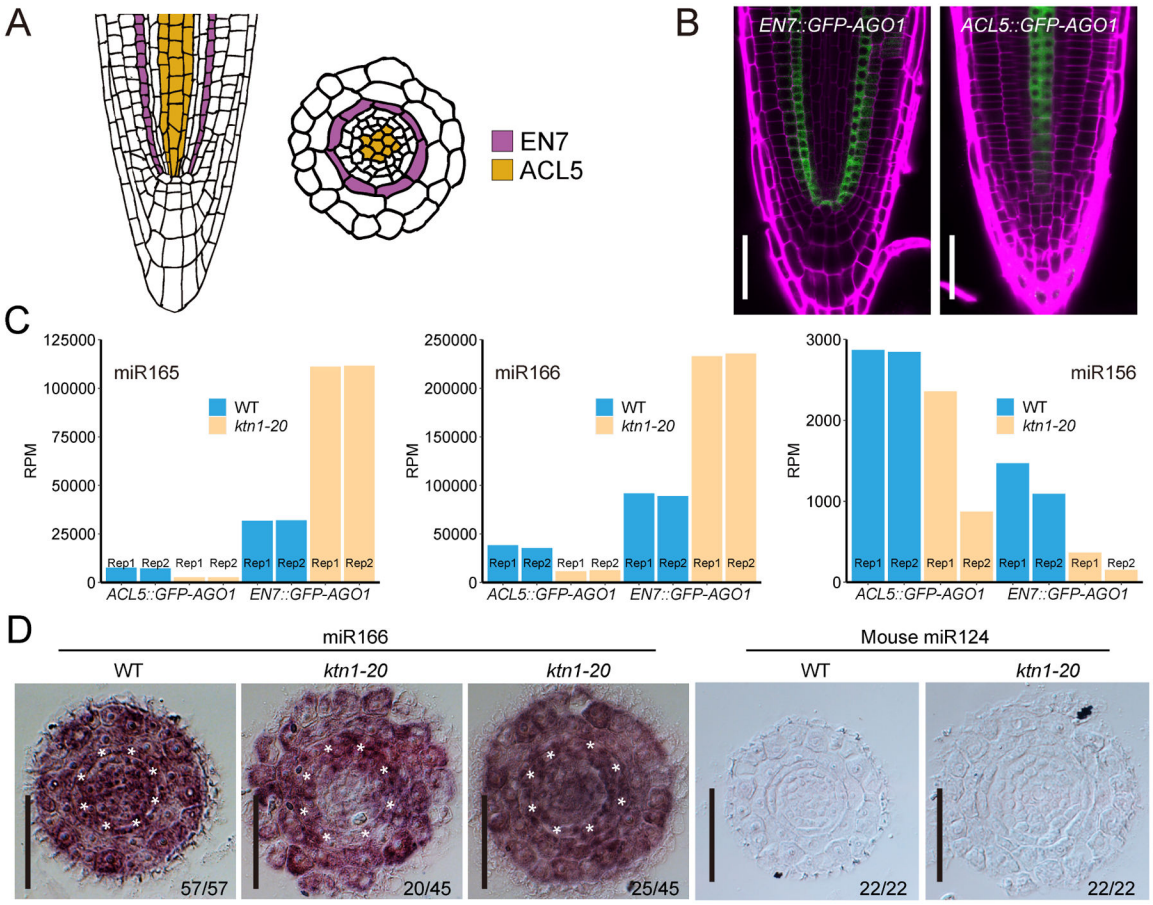


**Figure 6. AGO1 loading efficiency of miR165/6 in the endodermis and metaxylem.**

(A) Schematic representations of a longitudinal (left) and a cross (right) section of an *Arabidopsis* root. Endodermis, and metaxylem and procambia, where *GFP-AGO1* is specifically expressed, are colored. (B) Representative confocal GFP-AGO1 signals from *EN7::GFP-AGO1* and *ACL5::GFP-AGO1*. (C) Normalized read counts of miR165, miR166 and miR156 in small RNAseq of GFP-AGO1 IP from the indicated genotypes. Rep1 and 2 are two independent replicates. (D) In situ hybridization with a miR166-specific LNA probe on cross sections of WT and *ktn1-20* roots. An LNA probe against mouse miR124 was used as a negative control. Asterisks show the endodermis. The numbers represent the number of roots with the displayed pattern out of the total number of roots examined. Scale bars, 50 μm. See also Figure S5.

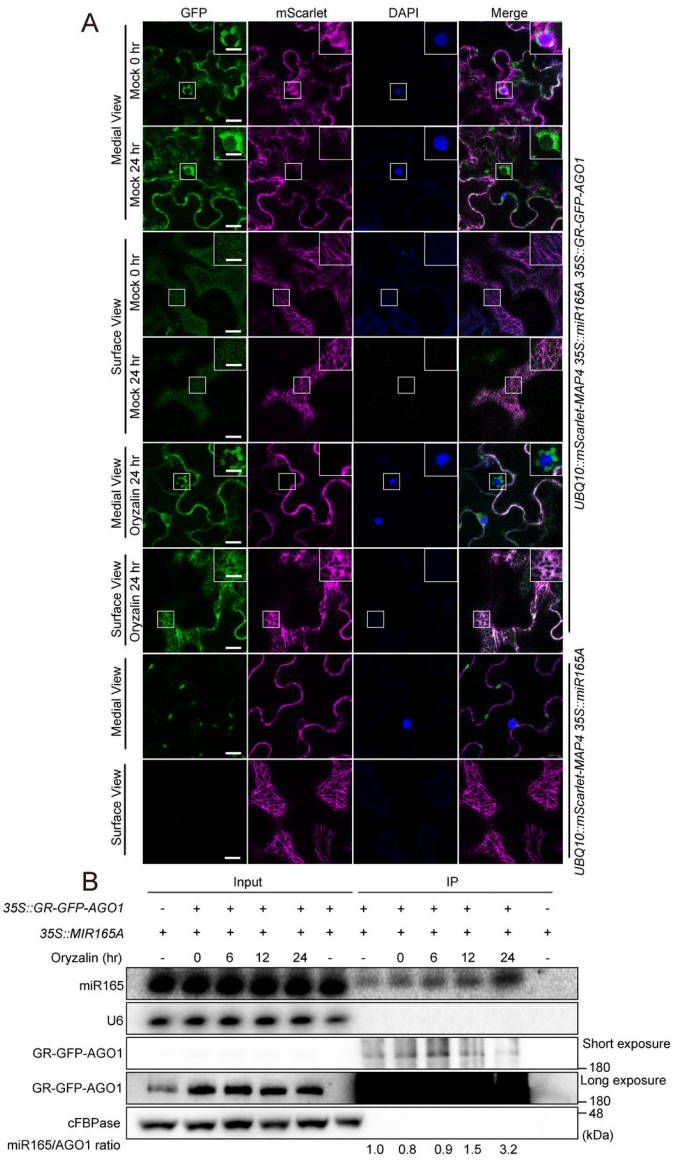


**Figure 7. MTs suppress the association of miR165 with AGO1 in the cytosol.**

(A) Confocal images of GR-GFP-AGO1 and mScarlet-MAP4 co-expressed transiently in *N. benthamiana* leaves. GR-GFP-AGO1 and mScarlet-MAP4 signals were examined before and after oryzalin treatment. Nuclei were stained by DAPI. Note that MTs were disrupted by oryzalin treatment. The medial views show the cytoplasmic localization of GR-GFP-AGO1 and the surface views show patterns of cortical MTs labeled by mScarlet-MAP4. Leaves infiltrated with *UBQ10::mScarlet-MAP4* and *35S::MIR165A* were used as negative controls. Scale bars, 20 μm. Insets, high magnification images. Scale bar, 10 μm in insets. (B) GR-GFP-AGO1 IP followed by RNA gel blot analysis to examine the association of miR165 with GR-GFP-AGO1 in the cytosol. The levels of miR165 in the immunoprecipitates were quantified against GR-GFP-AGO1 levels and shown below the gel images. *35S::MIR165A* without *GR-GFP-AGO1* was included as a control to show that miR165 signals in the IP samples represented miR165 bound by GR-GFPAGO1. The longer

exposure for the protein gel blot shows the signals of GR-GFP-AGO1 in input samples. See also Figure S6.

## KEY RESOURCES TABLE

| REAGENT or RESOURCE | SOURCE | IDENTIFIER |
|---|---|---|
| Antibody | | |
| Mouse monoclonal anti-GFP | Abcam | Cat#: ab290 |
| Rabbit polyclonal anti-AGO1 | Agrisera | Cat#: AS09527 |
| Rabbit polyclonal anti-AGO10 | Agrisera | Cat#: AS15 3071 |
| Rabbit polyclonal anti-SUL | Jia et al., 2017. | NA |
| Mouse monoclonal anti-HSC70 | Enzo life sciences | Cat#: ADI-SPA-818-F |
| Rabbit polyclonal anti-CFBPase | Agrisera | Cat#: AS04043 |
| Rabbit polyclonal anti-H3 | Abcam | Cat#: ab1791 |
| GFP-Trap®_MA | ChromoTek | Cat#: gtma-20 |
| Chemicals, Peptides, and Recombinant Proteins | | |
| Basic Fuschin | Sigma | Cat#: 215597 |
| DAPI | Sigma | Cat#: D9542 |
| Propidium iodide | Sigma | Cat#: P4170 |
| oryzalin | Sigma | Cat#: 36182 |
| TRI Reagent | MRC | Cat#: TR118 |
| DNase I | Sigma | Cat#: 04716728001 |
| Protease inhibitor cocktail | Roche | Cat#: 5056489001 |
| Critical Commercial Assays | | |
| ECL western blotting detection reagent | Cytiva Amersham | Cat#: RPN2232 |
| RevertAid Reverse Transcriptase | Thermo Fisher | Cat#: EP0442 |
| Deposited Data | | |
| Sequencing data have been deposited into GEO | This paper | GSE168805 |
| Experimental Models: Organisms/Strains | | |
| *Arabidopsis thaliana: ktn1–2* | Lin et al., 2008 | NA |
| *Arabidopsis thaliana: mor1-1* | Whittington et al., 2001 | NA |
| *Arabidopsis thaliana: SUC2::amiR-SUL* | de Felippes et al., 2011 | NA |
| *Arabidopsis thaliana: SUC2::amiR-SUL ktn1-20* | This paper | NA |
| *Arabidopsis thaliana: SUC2::amiR-SUL ktn1–2* | This paper | NA |
| *Arabidopsis thaliana: SUC2::amiR-SUL mor1-1* | This paper | NA |
| *Arabidopsis thaliana: SUC2::amiR-SUL KTN1::KTN1 ktn1–2* | This paper | NA |
| *Arabidopsis thaliana: pMIR165A::GFPer* | Miyashima et al.,2011 | NA |
| *Arabidopsis thaliana: pMIR165B::GFPer* | Miyashima et al.,2011 | NA |
| *Arabidopsis thaliana: pMIR166A::GFPer* | Miyashima et al.,2011 | NA |
| *Arabidopsis thaliana: pMIR166B::GFPer* | Miyashima et al.,2011 | NA |
| *Arabidopsis thaliana: pMIR165A::GFPer ktn1-20* | This paper | NA |
| *Arabidopsis thaliana: pMIR165B::GFPer ktn1-20* | This paper | NA |
| *Arabidopsis thaliana: pMIR166A::GFPer ktn1-20* | This paper | NA |

| REAGENT or RESOURCE | SOURCE | IDENTIFIER |
|---|---|---|
| *Arabidopsis thaliana: pMIR166B::GFPer ktn1-20* | This paper | NA |
| *Arabidopsis thaliana: PHB::PHB-GFP* | Miyashima et al.,2011 | NA |
| *Arabidopsis thaliana: PHB::PHB-GFP ktn1-20* | This paper | NA |
| *Arabidopsis thaliana: PHB::PHB-GFP mor1-1* | This paper | NA |
| *Arabidopsis thaliana: CRE1::miR165A* | Miyashima et al.,2011 | NA |
| *Arabidopsis thaliana: CRE1::miR165A ktn1-20* | This paper | NA |
| *Arabidopsis thaliana: CRE1::miR165A PHB::PHB-GFP* | This paper | NA |
| *Arabidopsis thaliana: CRE1::miR165A ktn1-20 PHB::PHB-GFP* | This paper | NA |
| *Arabidopsis thaliana: AGO1::GFP-AGO1* | This paper | NA |
| *Arabidopsis thaliana: AGO1::GFP-AGO1 ktn1-20* | This paper | NA |
| *Arabidopsis thaliana: EN7::GFP-AGO1* | This paper | NA |
| *Arabidopsis thaliana: ACL5::GFP-AGO1* | This paper | NA |
| *Arabidopsis thaliana: EN7::GFP-AGO1 ktn1-20* | This paper | NA |
| *Arabidopsis thaliana: ACL5::GFP-AGO1 ktn1-20* | This paper | NA |
| *Arabidopsis thaliana: EN7::KTN1 ktn1-20* | This paper | NA |
| *Arabidopsis thaliana: AHP6::KTN1 ktn1-20* | This paper | NA |
| *Arabidopsis thaliana: ACL5::KTN1 ktn1-20* | This paper | NA |
| *Arabidopsis thaliana: SHR::KTN1 ktn1-20* | This paper | NA |
| Oligonucleotides | | |
| Primers for probes and cloning see Table S1 | This paper | NA |
| Recombinant DNA | | |
| *CRE1::miR165A* | Miyashima et al.,2011 | NA |
| *AGO1::GFP-AGO1* | This paper | NA |
| *KTN1::KTN1* | This paper | NA |
| *EN7::GFP-AGO1* | This paper | NA |
| *ACL5-GFP-AGO1* | This paper | NA |
| *EN7::KTN1 ktn1-20* | This paper | NA |
| *AHP6::KTN1 ktn1-20* | This paper | NA |
| *ACL5::KTN1 ktn1-20* | This paper | NA |
| *SHR::KTN1 ktn1-20* | This paper | NA |
| *35S::GR-GFP-AGO1* | This paper | NA |
| *35S::miR165A* | This paper | NA |
| *UBQ10::mScarlet-MAP4* | Pan et al. 2020 | NA |